Air and PCM cooling for battery thermal management considering battery cycle life

Chen, F., Huang, R., Wang, C., Yu, X., Liu, H., Wu, Q., Qian, K. & Bhagat, R.

Author post-print (accepted) deposited by Coventry University's Repository

Original citation & hyperlink:
Chen, F, Huang, R, Wang, C, Yu, X, Liu, H, Wu, Q, Qian, K & Bhagat, R 2020, 'Air and PCM cooling for battery thermal management considering battery cycle life', Applied Thermal Engineering, vol. 173, 115154.
https://dx.doi.org/10.1016/j.applthermaleng.2020.115154

DOI 10.1016/j.applthermaleng.2020.115154
ISSN 1359-4311

Publisher: Elsevier

NOTICE: this is the author's version of a work that was accepted for publication in Applied Thermal Engineering. Changes resulting from the publishing process, such as peer review, editing, corrections, structural formatting, and other quality control mechanisms may not be reflected in this document. Changes may have been made to this work since it was submitted for publication. A definitive version was subsequently published in Applied Thermal Engineering, 173, (2020) DOI: 10.1016/j.applthermaleng.2020.115154

© 2020, Elsevier. Licensed under the Creative Commons Attribution-NonCommercial-NoDerivatives 4.0 International http://creativecommons.org/licenses/by-nc-nd/4.0/

Copyright © and Moral Rights are retained by the author(s) and/ or other copyright owners. A copy can be downloaded for personal non-commercial research or study, without prior permission or charge. This item cannot be reproduced or quoted extensively from without first obtaining permission in writing from the copyright holder(s). The content must not be changed in any way or sold commercially in any format or medium without the formal permission of the copyright holders.

This document is the author's post-print version, incorporating any revisions agreed during the peer-review process. Some differences between the published version and this version may remain and you are advised to consult the published version if you wish to cite from it.

Air and PCM Cooling for Battery Thermal Management Considering Battery Cycle Life

Fenfang Chen[a], Rui Huang[a], Chongming Wang[c*], Xiaoli Yu[a*], Huijun Liu[a, b], Qichao Wu[a], Keyu Qian[a], Rohit Bhagat[c]

[a] *College of Energy Engineering, Zhejiang University, Hangzhou, China, 310027*
[b] *Zotye Automotive Engineering Research Institute, Hangzhou, China, 310018*
[c] *Institutes of Future Transport and Cities, Coventry University, Coventry, United Kingdom, CV1 5FB*

[*] Corresponding author *e-mail address*: ac8174@coventry.ac.uk (Dr Chongmign Wang); yuxl@zju.edu.cn (Prof Xiaoli Yu)

Highlights

- Performance of air and PCM battery cooling is studied.
- Realistic charge/discharge current profile is applied in simulations.
- Battery non-uniform degradation and battery cycle life are analysed.
- A performance index for assessment of battery thermal management system is proposed.

Abstract

Cycle life of lithium-ion batteries (LIBs) is essential for the application of hybrid electric vehicles (HEV) and electric vehicles (EV). Since temperature greatly affects degradation rate and safety of LIBs, battery thermal management system (BTMS) is required. In this paper, the performance of active air cooling and passive phase change material (PCM) cooling for BTMS are assessed in terms of battery thermal states and cycle life. A coupled one-dimensional electrochemical and two-dimensional thermal models are developed to simulate the temperature of a battery module with 16 cylindrical (26650) graphite-$LiFePO_4$ lithium-ion battery cells. The model is validated with the experimental data taken from literature. By applying a realistic current profile of a HEV to the battery model, simulations are performed at various ambient temperatures, inlet velocities of air cooling and PCM phase change temperatures. The battery cycle life and its non-uniformity across the module are estimated with a battery degradation model with inputs of battery temperature results. The study shows that active air cooling has a better cooling effect than PCM cooling, especially at high ambient temperatures. But the active air cooling leads to a large temperature non-uniformity at low inlet air velocities. The cycle life of the battery module under air cooling is longer than that of PCM cooling, although a larger life non-uniformity is observed. Furthermore, two methods are compared by a newly proposed evaluation index called cyclical cost. This index considers both the battery cycle life and the parasitic power consumption of the BTMS. The result demonstrates that air cooling has a lower cyclical cost than PCM cooling. When the inlet velocity of the air cooling system increases, the cyclical cost has a trend of decreasing first and then increasing. This paper provides a guide for the development of BTMS to further prolong the cycle life and reduce total operating cost of LIBs.

Keywords: Lithium-ion battery; thermal management; air cooling; PCM cooling; cycle life

Greek symbols

α	Transfer coefficient
γ	Bruggeman tortuosity exponent
δ	Cyclical cost (€ cycle^{-1})
ε	Volume fraction
ζ_N	Maximum cycle life difference rate
η	Local surface over potential (V)
θ	Capacity loss (%)
λ	Thermal conductivity (W m^{-1} K^{-1})
ρ	Density (kg m^{-3})
σ	Electronic/ionic conductivity (S m^{-1})
τ	Price (€)
Φ	Potential (V)
Δ	Change
∇	Divergence

Symbols

A_{cell}	Area of the positive electrode (both sides) (m^2)
c	Lithium-ion concentration (mol m^{-3})
$C_{p,i}$	Heat capacity (J kg^{-1} K^{-1})
D_i	Diffusion coefficient (m^2 s^{-1})
F	Faraday's constant (C mol^{-1})
h	Heat transfer coefficient (W m^{-2} K^{-1})
H	Enthalpy (J kg^{-1})
H_{fuel}	Lower heating value of the fuel (J L^{-1})
I	Current (A)
i	Current density (A m^{-2})
j_n	Local charge transfer current density (A m^{-2})
j_0	Exchange current density (A m^{-2})
k_0	Reaction rate constant (m$^{2.5}$ mol$^{-0.5}$ s^{-1})
L_i	Thickness of component (m)
N	Number of cycle before end of life
$\overline{N}$	Mean cycle life of the module
ΔN	Maximum cycle life difference across the module
P	Power (W)
p	Pressure (Pa)
q	Total heat generation (J m^{-3})
q_{act}	Active heat generation (J m^{-3})
q_{ohm}	Ohmic heat generation (J m^{-3})
q_{rea}	Reaction heat generation (J m^{-3})
r	Radius distance variable of particle (m)
R	Characteristic radius of electrode particles (m)
R_{gas}	Gas constant (J mol^{-2} K^{-1})
S_a	Specific surface area (m^{-1})
t	Time (s)
t_+	Li$^+$ transference number

T	Temperature (℃)
ΔT	Maximum temperature difference (℃)
U_{eq}	Open circuit potential of the electrode (V)
U_i	Open circuit voltage (V)
v	Thermodynamic factor
V_{in}	Inlet velocity (m s^{-1})

Subscripts

0	Initial or equilibrated state
1	Solid phase
2	Liquid/electrolyte phase
n	Negative electrode
s	Separator
p	Positive electrode
air	Air
amb	Ambient
AC	Air conditioner
batt	Battery
eff	Effective value
fan	Fan
fuel	Fuel
max	Maximum
pcm	Phase change material
ref	Reference value
surf	Surface of active material

Abbreviations

BTMS	Battery thermal management system
EV	Electric vehicle
HEV	Hybrid electric vehicle
LIB	Lithium ion battery
PCM	Phase change material
PCT	Phase change temperature
SOC	State of charge

1. Introduction

Air pollution, global climate change and fossil energy shortage are the major driven forces behind the development of the energy and transportation sectors. In the automobile industry, traditional engine-powered vehicles are gradually replaced by hybrid electric vehicles (HEVs) and electric vehicles (EVs) [1]. For the energy storage system in HEVs/EVs, lithium-ion batteries (LIBs) are widely used for its high voltage, high energy density, and low self-discharge rate.

Even though LIBs are the best energy storage system so far, they still have some drawbacks, such as degradation [2], low energy density compared with internal combustion engines [3] and high cost [4]. Low energy density limits the driving mileage of HEV/EVs. Degradation further reduces driving mileage and causes range anxiety, and it also increases the operating cost of HEV/EVs if it needs replacement. Approximately 50% of the vehicle cost is from the battery pack. In addition, recycling of LIBs is another challenging issue that has not been solved [5]. Therefore, reducing battery degradation rate and improving the cycle life of LIBs are of great relevance for future clean transportation. There are two research directions in this area. One is technology advancement in battery cells, such as new material [6], material modification [7] and the improvement of manufacture technology. The other is battery management, including but not limited to, online fault diagnosis [8,9], equalization control [10,11] and thermal management. Battery thermal management has been received increasing attention since the temperature is one of the most sensitive factors to battery cycle life. More importantly, high temperature may lead to the risk of battery thermal runaway.

Studies of battery thermal management have been carried out to control the temperature of LIBs, from basic air cooling systems to compound systems like PCM and heat pipe compound battery thermal management system (BTMS) [12–16]. In addition, novel thermal management methods are reported [17,18]. The main goal of these studies is to control the temperature of LIBs within the safety range for avoiding battery thermal runaway. However, even the temperature of the LIBs has been controlled under the threshold of the thermal runaway, the temperature still has a great impact on battery cycle life. Experimental tests [19] show that the cycle life of the battery cell reduced by 50% if the temperature rises from 25 °C to 45 °C [19]. Neubauer et al. [20] of National Renewable Energy Laboratory examined the sensitivity of electric vehicle battery pack degradation to battery thermal management. The battery life was estimated when it was cooled by a passive system and a powerful liquid cooling system with three different operation modes (key-on, standby and combined). The results show that applying liquid cooling systems can significantly reduce capacity loss and resistance growth

rate, and combined key-on and standby system offered best reduction in degradation. Yuksel et al. [21] assessed the influence of thermal management on battery degradation. The battery life was simulated under the conditions of with and without air-cooling system. Applying an air-cooling system doubled life compared with no BTMS.

However, the existing studies looked mainly at the impacts and sensitivities of various factors on battery life, and thermal management is one of the many factors. Heat generation and heat transfer processes were modelled by using lumped parameter method, which only solved the average temperature of the whole battery pack rather than temperature distributions. Therefore, indexes of temperature non-uniformity and degradation non-uniformity were not obtained. Meanwhile, BTMS investigated in these studies were limited to several specific scenarios, and the influences of BTMS parameters on battery cycle life has not been studied.

The novelty of this paper is that it quantitatively evaluates the degradation characteristics, including cycle life and its non-uniformity across the module, of the battery module under different cooling configurations. There is limited literature covering this area, however, it is of great significance for BTMS. Since extending battery cycle life is one of the purposes of battery thermal management, the authors think that battery life should must be considered as one of the indexes of BTMS. However, the previous studies mainly take battery maximum temperature, temperature non-uniformity and power consumption as evaluation indexes for BTMS. Hence, this study proposed a battery health-conscious evaluation index for BTMS, which considers both power consumption of BTMS and cycle life of batteries. The simulation results and newly proposed evaluation index can provide new ideas for battery health-conscious thermal management.

In this study, a one-dimensional electrochemical model is developed for the lithium-ion battery cell in COMSOL, a multi-physics modelling software, where the heat generation can be solved accurately. Then, a two-dimensional thermal model is developed in COMSOL to simulate the heat transfer processes in the battery pack. The electrochemical and thermal models are coupled together via heat generation and temperature. The model is validated using experimental data from the literature. The simulation is carried out by using realistic current load and thermal management methods of active air cooling and passive phase change material (PCM) cooling are involved. On this basis, the time-varying temperature field of the module can be obtained. The degradation process of the battery cell is assessed by a battery capacity loss model. The effects of ambient temperatures, inlet velocities of air cooling and PCM phase change temperatures are studied.

2. Model development

2.1 Electrochemical model

In this study, a one-dimensional electrochemical model developed by Doyle and Newman [22,23] is used to predict heat generation of LIBs. This model is widely published in literature [24–26] and will therefore not be repeated here. The governing equations are provided in Table 1 for completeness. A cylindrical type of the graphite-$LiFePO_4$ battery manufactured by A123 system (ANR26650M1A) is chosen in this study. Fig. 1(a) and Fig. 1(b) show the internal structure of the battery cell and the schematic of the computational domain of the one-dimensional electrochemical model, respectively. The positive and negative current collectors are neglected in our study. Geometrical and design parameters, kinetic and transport properties, and thermal properties of the battery used for modelling are listed in Table 2.

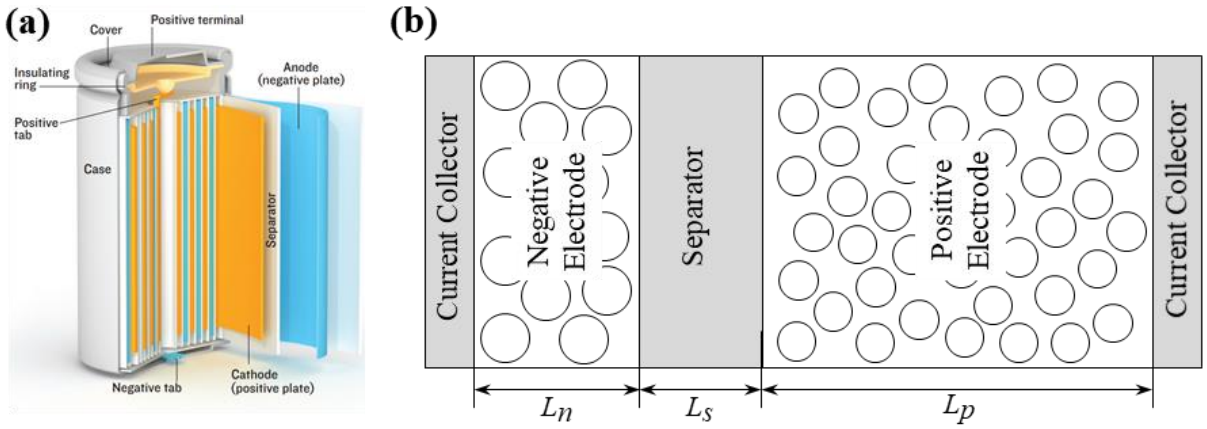

Fig. 1 Internal structure of the battery cell (a) [27] and the schematic of the computational domain (b)

Table 1: Governing equations for the 1-D electrochemical model

Description	Governing equations
Electrochemical kinetics	$j_n = j_0 \left\{ \exp\left(\frac{\alpha_a F}{R_{gas} T} \eta \right) - \exp\left(-\frac{\alpha_c F}{R_{gas} T} \eta \right) \right\}$
	$j_0 = F k_0 c_2^{\alpha_a} \left(c_{1,\max} - c_{1,surf} \right)^{\alpha_a} c_{1,surf}^{\alpha_c}$
	$\eta = \phi_1 - \phi_2 - U_{eq}$
	$U_{eq,i} = U_{ref,i} + \frac{\partial U_{eq,i}}{\partial T} \left(T - T_{ref} \right)$
	$= U_{ref,i} \left(SOC, T_{ref} \right) + \frac{\Delta S_i \left(SOC \right)}{F} \left(T - T_{ref} \right)$

	$SOC = \frac{c_i}{c_{i,\max}}$
Charge conservation	$\nabla \cdot i_1 + \nabla \cdot i_2 = 0$
	$\nabla \cdot i_1 = -S_a j_n$
	$\nabla i_2 = S_a j_n$
	$i_1 = -\sigma_1^{eff} \nabla \phi_1$
	$i_2 = -\sigma_2^{eff} \nabla \phi_2 + \frac{2R_{gas} T \sigma_2^{eff}}{F}\left(1 + \frac{\partial \ln f_{\pm}}{\partial \ln c_2}\right)(1 - t_+)\nabla(\ln c_2)$
Mass conservation	$\frac{\partial c_1}{\partial t} = \frac{1}{r^2}\frac{\partial}{\partial r}\left(-r^2 D_1 \frac{\partial c_1}{\partial r}\right)$
	$\varepsilon_2 \frac{\partial c_2}{\partial t} + \nabla \cdot J_2 = \frac{S_a j_n}{F}$
	$\varepsilon_2 \frac{\partial c_2}{\partial t} + \nabla \cdot J_2 = \frac{S_a j_n}{F}$
Energy conservation	$q_{rea} = S_a j_n T \frac{\partial U_i}{\partial T}$
	$q_{act} = S_a j_n \eta$
	$q_{ohm} = -i_1 \cdot \nabla \phi_1 - i_2 \cdot \nabla \phi_2$
	$q = q_{rea} + q_{act} + q_{ohm}$

Table 2: Main parameter of ANR26650M1A type LiFePO4 cylindrical battery

Parameter	Positive	Separator	Negative
nominal capacity (Ah)		2.3	
Cell radius (m)		0.013	
Cell height (m)		0.065	
A_{cell} (m^2)		0.18[a]	
L_i (m)	8.0×10^{-5}[a]	2.5×10^{-5}[a]	3.4×10^{-5}[a]
R_i (m)	5×10^{-8}[a]	-	5×10^{-6}[a]
$\varepsilon_{1,i}$	0.374[a]	-	0.58[a]
$\varepsilon_{2,i}$	0.444[a]	0.54[b]	0.357[a]
$c_{1,i}$ (mol m^{-3})	22806×0.03[b]		30555×0.8[b]
$c_{2,0}$ (mol m^{-3})	1200[b]	1200[b]	1200[b]
$c_{1,max}$ (mol m^{-3})	22806[a]	-	30555[a]
α_a, α_c	0.5[a]	-	0.5a
γ_i	1.5[a]	1.5[a]	1.5a

$U_{ref,i}$	Fig. 1A(a) [c]		Fig. 1A(a) [c]
ΔS_i	Fig. 1A(b) [d]		Fig. 1A(b) [e]
σ_1 (S m^{-1})	0.5[b]	-	100[b]
σ_2 (S m^{-1})	Fig. 2A [a]		
$D_{1,p}$ (m^2 s^{-1})	$D_{1,p}(T)=1.18\times10^{-18}\exp\left[\frac{39000}{R}\left(\frac{1}{T_{ref}}-\frac{1}{T}\right)\right]$ [a,b]		
$D_{1,n}$ (m^2 s^{-1})	$D_{1,n}(T)=3.9\times10^{-14}\exp\left[\frac{35000}{R}\left(\frac{1}{T_{ref}}-\frac{1}{T}\right)\right]$ [a,b]		
D_2 (m^2 s^{-1})	2.0×10^{-10}[a]		
$k_{0,p}$ (m$^{2.5}$ mol$^{-0.5}$ s^{-1})	$k_{0,p}(T)=3\times10^{-11}\times\exp\left[\frac{30000}{R}\left(\frac{1}{T_{ref}}-\frac{1}{T}\right)\right]$ [b]		
$k_{0,n}$ (m$^{2.5}$ mol$^{-0.5}$ s^{-1})	$k_{0,n}(T)=1.4\times10^{-12}\times\exp\left[\frac{20000}{R}\left(\frac{1}{T_{ref}}-\frac{1}{T}\right)\right]$ [b]		
ν	$\nu=0.601-0.24\sqrt{10^{-3}c}+0.982\left(1-0.0052(T-294.0)\sqrt{10^{-9}c^3}\right)$		
t_+	0.363[b]		
Thermal conductivity (W m^{-1} K^{-1})	0.2[b]		
Heat Capacity (J kg^{-1} K^{-1})	1100[a]		
Density (kg m^{-3})	2047[a]		
T_{ref} (K)	298.15		
R_{gas} (J mol^{-2} K^{-1})	8.314		
F (C mol^{-1})	96,487		

[a] Ref.[25]; [b] Ref.[26]; [c] Ref.[28]; [d] Ref.[29]; [e] Ref.[30]

2.2 Thermal model

For the simplicity of numerical simulation, thermal radiation in the whole model is neglected. Besides, because there is no liquid motion existing in paraffin-graphite composite (thus, its viscosity is regarded as 10^5 kg m^{-1} s^{-1}) [31], the momentum equation is not considered for the melted PCM [31,32]. Therefore, the only one governing equation of both battery cell and PCM domains is the energy conservation equation:

$$\rho_i C_{p,i}\frac{\partial T}{\partial t}=\nabla\left(\lambda_i\nabla T\right)+q_i \quad (1)$$

where the subscript i refers to battery cell or PCM; q_i is the heat source term. In the domain of battery cells, q_i is the total heat generation coming from the 1-D electrochemical model. The average temperature of the battery cell calculated by Eq.(1) is used for 1-D electrochemical model. In the domain of PCM, the value of q_i is 0. Equivalent heat capacity method is employed to take the melting

latent heat of PCM into account, with which the apparent heat capacity of the PCM during phase transition is defined as:

$$C_{p,pcm} = C_{eq} + C_L(T) \tag{2}$$

where C_{eq} is the equivalent heat capacity of the solid-liquid mixture; $C_L(T)$ is the latent heat distribution within phase transition interval.

In the domain of cooling air, fluid flow and heat transfer are governed by the continuity, momentum conservation and energy conservation equations:

$$\frac{\partial \rho_{air}}{\partial t} + \nabla \cdot (\rho_{air} \vec{v}) = 0 \tag{2}$$

$$\frac{\partial (\rho_{air} \vec{v})}{\partial t} + \nabla \cdot (\rho_{air} \vec{v}\vec{v}) = -\Delta p \tag{3}$$

$$\frac{\partial (\rho_{air} C_{p,air} T)}{\partial t} + \nabla \cdot (\rho_{air} C_{p,air} \vec{v} T) = \nabla \cdot (\lambda_{air} \nabla T) \tag{4}$$

Temperature and heat flux are continuous at the interface of PCM/cell and air/cell, where the energy conservation equation can be expressed as:

$$\lambda_{batt} \frac{\partial T}{\partial n} = \lambda_{pcm} \frac{\partial T}{\partial n} \tag{5}$$

$$\lambda_{batt} \frac{\partial T}{\partial n} = h(T_{batt} - T_{air}) \tag{6}$$

In PCM cooling condition, PCM is cooled by ambient air in the way of natural convection, the governing equation is:

$$\lambda_{pcm} \frac{\partial T}{\partial n} = h_{natural}(T_{pcm} - T_{amb}) \tag{7}$$

2.3 Battery Degradation model

The battery degradation is reflected in capacity loss and impedance rise. Here, we only consider the capacity loss of LIBs. Wang et al. [33] developed a capacity loss model for ANR26650M1A (the same with the one studied in this paper) by carrying out a serious of experiments. In their model, the relationship between capacity loss and the temperature is formulated with an Arrhenius type equation. The generic capacity degradation model given by Wang et al. is expressed as follows:

$$\theta^{CYC} = A \cdot \exp\left(\frac{-31700 + 370.3 \times \left(I^{CELL} / C_{nom}^{CELL}\right)}{R \cdot T^{CELL}}\right) Ah^{0.55} \tag{8}$$

where θ^{CYC} is the capacity loss; A is a constant for given current and its values are listed in Table 3; I^{CELL} is the charge/discharge current; C_{nom}^{CELL} is the nominal capacity of the cell; I^{CELL}/C_{nom}^{CELL} is the charge/discharge rate (C_{rate}); T^{CELL} is the cell temperature and Ah is the total Ah-throughput.

In the dynamic cycling assessment of this study, it is assumed that during a very short time step from t to $t+\Delta t$, the charge/discharge current and cell temperature remain unchanged. The accumulated capacity loss at a time $t+\Delta t$ can be expressed as follows:

$$\theta_{t+\Delta t}^{CYC} = \Gamma_{t+\Delta t} \cdot \left[\left(\frac{\theta_t^{CYC}}{\Gamma_{t+\Delta t}}\right)^{\frac{1}{0.55}} + \Delta Ah_{t+\Delta t}\right]^{0.55} \tag{9}$$

$$\Gamma_{t+\Delta t} = A_{t+\Delta t} \cdot \exp\left(\frac{-31700 + 370.3 \times C_{rate,t+\Delta t}^{CELL}}{R \cdot T_{t+\Delta t}^{CELL}}\right) \tag{10}$$

where $\Delta Ah_{t+\Delta t}$ is the ampere-hour processed during time step Δt, which can be calculated as:

$$\Delta Ah_{t+\Delta t} = \int_t^{t+\Delta t} I^{CELL}(t) \cdot dt \cong \frac{1}{2}\left(|I_t^{CELL}| + |I_{t+\Delta t}^{CELL}|\right) \cdot \Delta t \tag{11}$$

$A_{t+\Delta t}$ is considered as a constant in each time step Δt, the value of which is estimated by linear interpolation between the tabulated values in Table 3.

Table 3: Values of coefficient A in Eq.(8)

C_{rate}	1/2	2	6	10
A	31,630	21,681	12,934	15,512

In addition, during the capacity loss assessment, we also have following simplifications: (1) The ageing mechanisms are the same during charge and discharge; (2) The capacity loss during storage (calendar life) is neglected.

In the process of simulation, the temperature profile of each cell in dynamic cycling can be calculated by the thermal model, and current profile is the input parameter of the electrochemical model. Based on temperature and current profiles, the accumulated capacity loss of cells can be solved by using the abovementioned capacity degradation model.

2.4 Model Validation

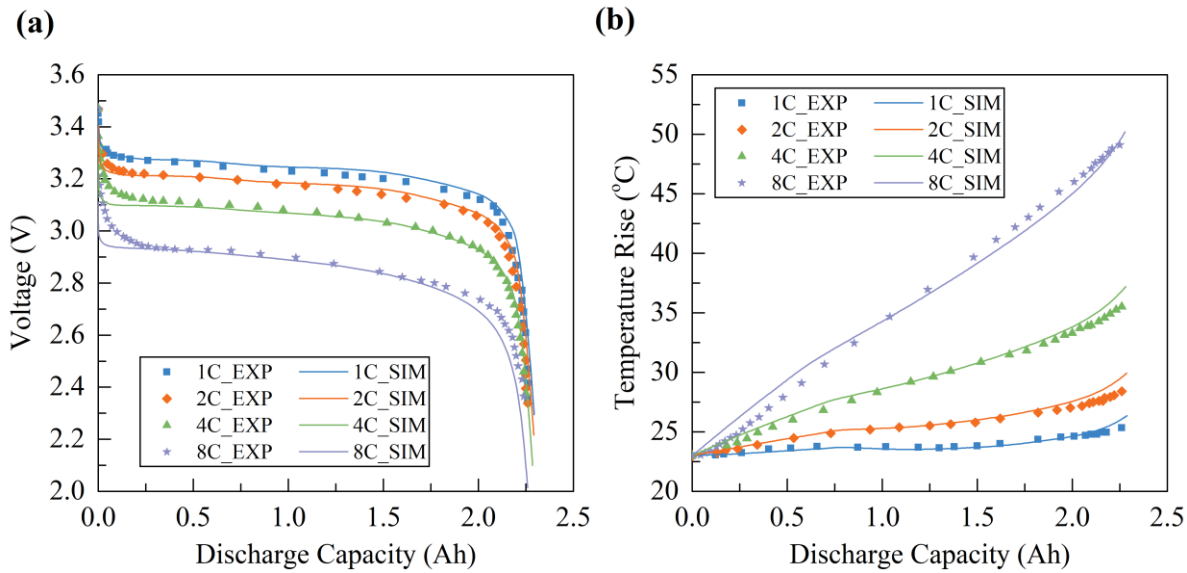

Fig. 2 Comparison of simulated results with the experimental data from literature: (a) Cell voltage and (b) surface temperature.

Fig. 2 shows the simulated results of cell voltage and surface mean temperature, along with experimental results published in Ref. [25]. The boundary conditions used in the simulation are the same with experimental conditions. Natural heat transfer coefficient ($h_{natural}$) of the cell surface is set as 10 W m^{-2} K^{-1} [25,34]. Fig. 2 shows that experimental data and simulated results match well, indicating the electro-thermal model is able to simulate battery thermal performance at different discharge rate.

3. Cooling configurations and simulation setup

Fig. 3 shows a battery module with 16 cells is selected for this study. In the air cooling BTMS, the cooling air is sent from the left side of the module (inlet) to the right side (outlet) through the gaps between battery cells and an optimized gap size of 7 mm is adopted according to Ref. [35]. In the PCM based BTMS, the gaps are filled with PCM. In general, the mass of the PCM can be estimated by the equation as follows [36]:

$$Q_{batt} = m_{pcm} \cdot C_{p,pcm} \cdot \left(PCT - T_{initial}\right) + m_{pcm} \cdot L \tag{13}$$

where Q_{batt} is the total heat generation of the battery, m_{pcm}, PCT, $T_{initial}$, L is the mass, phase change temperature, initial temperature and latent heat of PCM, respectively. Because the value of $C_{p,pcm}$ is much lower than L and $T_{initial}$ (T_{amb}) is one of the variables, the first item on the right side of Eq. (14) is not considered. Then a minimum m_{pcm} of 24.02 g $cell^{-1}$ (corresponding gap size between cells is

about 5 mm) can be obtained according to the battery heat generation and thermo-physical properties of PCM (see below). On this basis, the PCM based BTMS is assumed to have a same gaps size (7 mm) as the air cooling BTMS, which makes it work better.

A grid independence study is carried out to decide a proper element size. The temperature of a probe point on battery surface and total heat rate at the outlet are used to test the grid independence. Fig. 4 shows that the values of the two selected parameters. It is found that the results stabilize when the grid number reaches 27776, corresponding element size of 1 mm. Thus, element size of 1 mm is used in later study. Fig. 5(a) and Fig. 5(b) show the overall grid structure of the computational domain and the refined mesh at the interface of battery cells and cooling air.

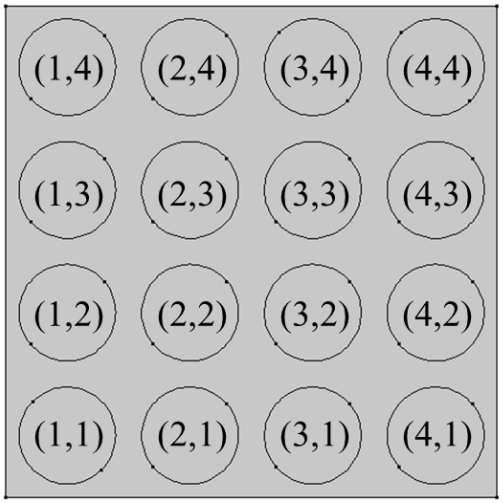

Fig. 3 Geometry of the battery pack

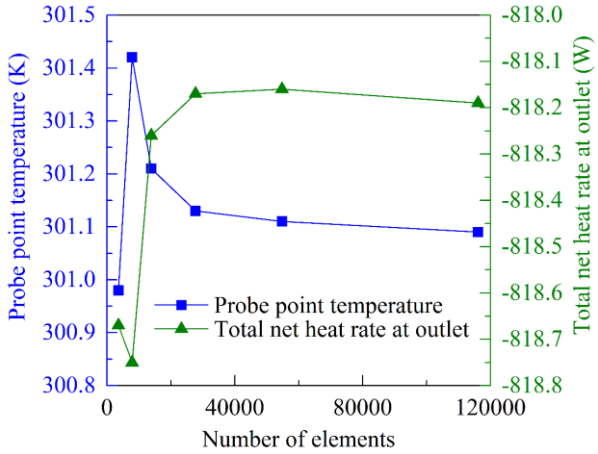

Fig. 4 Grid independent study

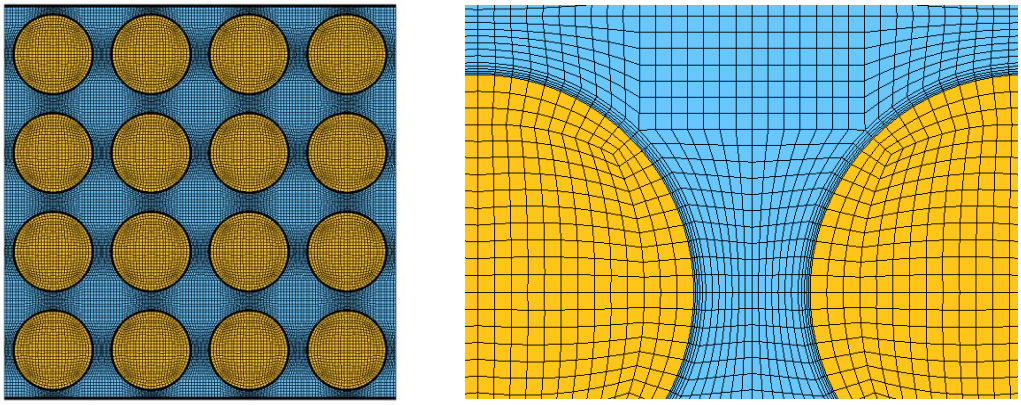

Fig. 5 2D Mesh of the battery module: (a) overall grid structure and (b) refined mesh at the interface of air and the battery cell.

Fig. 6 shows the current profile of ANR26650M1A selected in this study. This profile is the simulation result based on a hybrid electric bus and the total driving time and distance of the cycle are approximately 3000 s and 16.55 km, respectively [37]. It's defined that the discharge current is positive. The average heat generation rate under this load at 30 ℃ is 1.43 W cell^{-1}, which is equal to that under 4.25 C-constant current discharge.

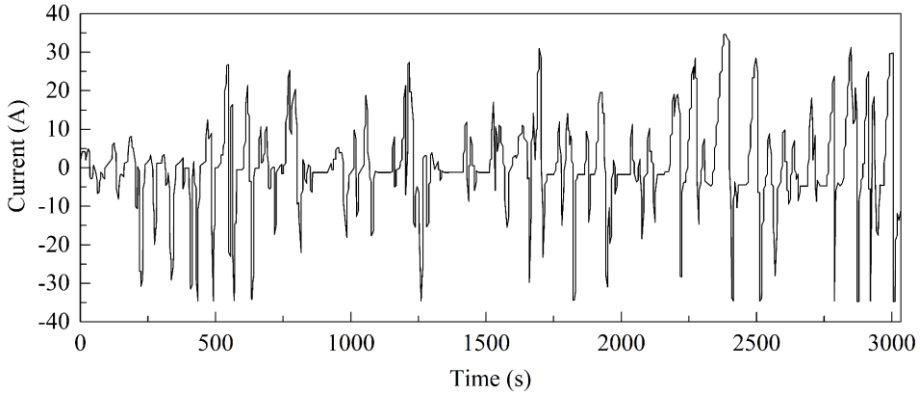

Fig. 6 Current profile of battery cells obtained from literature (Ref. [37])

In the study of air cooling, the battery pack is cooled by either 20 °C air-conditioned air when the ambient temperature (T_{amb}) is higher than 20 °C, or directly cooled by ambient air when T_{amb} is equal to or below 20 °C. The inlet velocity (V_{in}) is swept from 0 to 8 m s^{-1}, and T_{amb} swept from 0 and 50 °C. Table 4 lists the simulation boundary conditions/settings for air cooling cases.

Table 4: Simulation setup for air cooling cases

Type	Setting
Fluid dynamic conditions	Turbulence
Turbulence model	k-epsilon [35,38]

Inlet velocity [m s^{-1}]	0, 0.5, 1, 2, 3, 4, 6, 8
Inlet temperature [°C]	T_{amb} > 20 °C; T_{in} = 20 °C T_{amb} ⩽ 20 °C; T_{in} = T_{amb}
Outlet gauge pressure [Pa]	0
Wall of the module	Symmetry
Wall of the cell	Fluid-solid coupling
Ambient temperature [°C]	0, 10, 20, 30, 40, 50

Instead of taking heat away from the module by cooling medium in active BTMS, passive PCM based BTMS controls the battery temperature by accumulating or discharging heat of PCM and only part of the heat is dissipated to the ambient through sides of the module. Therefore, thermo-physical properties of the PCM and heat transfer boundary conditions of the module sides are important. In this study, a paraffin-graphite composite PCM [39] with relatively large thermal conductivity is chosen [40,41], which helps to dissipate the heat from the surface of battery cells to the side of the module and achieve an uniform temperature field. Two sides of the module are modelled as natural convection air cooling with a $h_{natural}$ of 10 W m^{-2} K^{-1} [25,34] and the others are symmetry. Then, the effect of PCT to battery thermal states and life is investigated, whilst the other thermo-physical properties of PCM, such as latent heat, specific heat capacity and transition interval, are kept constant. The T_{amb} is swept from 0 °C to 50 °C. Table 5 and Table 6 list the boundary conditions of the model and thermo-physical properties of PCM, respectively.

Table 5: Boundary conditions for PCM cooling cases

Type	Boundary condition
Sides of the module	Symmetry; natural heat transfer
Heat transfer coefficient [W m^{-2} K^{-1}]	10 [25,34]
Wall of the cell	Conduction
Ambient temperature [°C]	0, 10, 20, 30, 40, 50

Table 6: Thermo-physical properties of PCM [39]

parameter	Value/range
Latent heat [J kg^{-1}]	181000
Specific heat capacity [J kg^{-1} K^{-1}]	1980
Thermal conductivity [W m^{-1} K^{-1}]	16.6
Density [kg m^{-3}]	866
Transition interval [°C]	3
Phase change temperature [°C]	35, 40, 45, 50, 55

4. Results and discussion

The results and discussion are divided to three sub-sections, including the results of air cooling and PCM cooling, and the comparison of air cooling and PCM cooling.

4.1 Air cooling

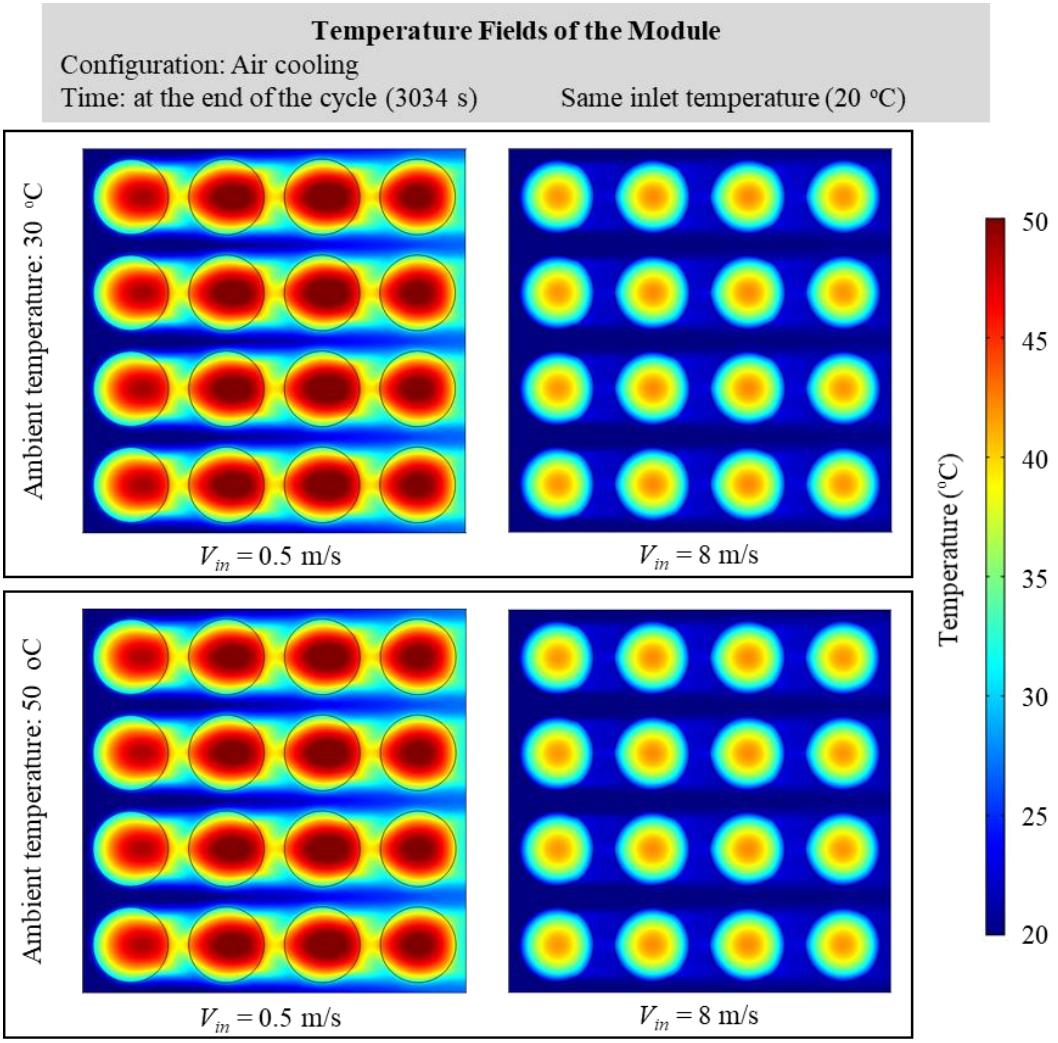

Fig. 7 Temperature fields of battery module at the end of the driving cycle

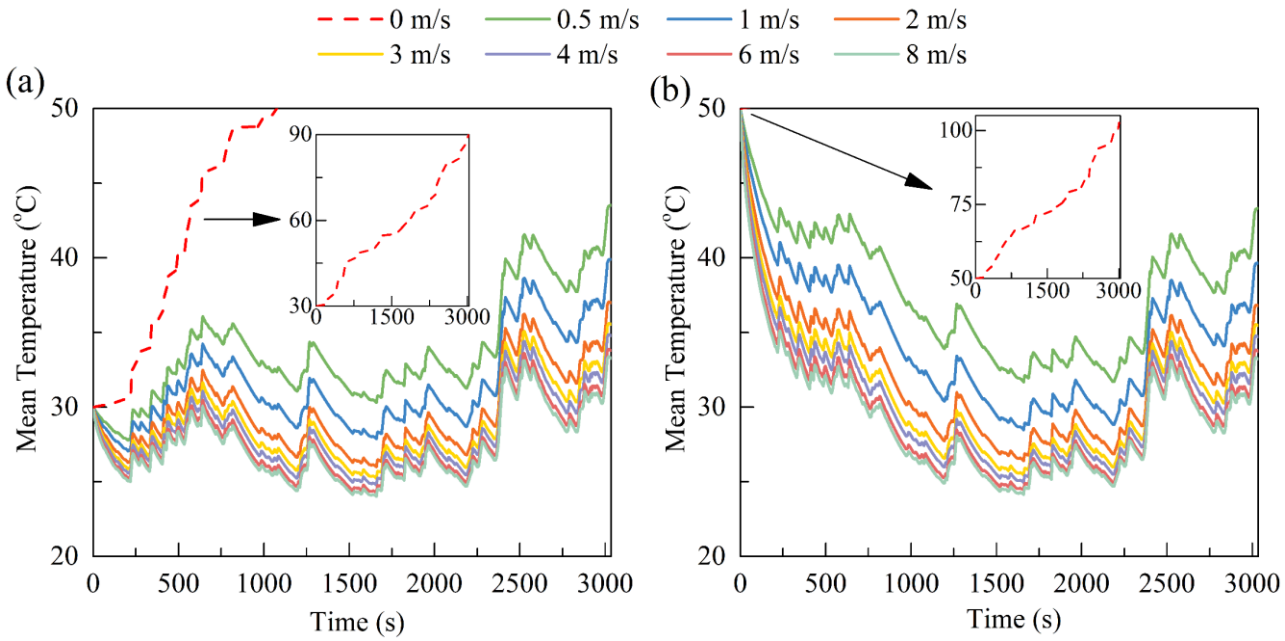

Fig. 8 Module mean temperature curves through the whole cycle: (a) T_{amb}=30 °C and (b) T_{amb}=50 °C

Fig. 7 and Fig. 8 and presents the temperature fields of battery module at the end of the driving cycle and the mean temperature of all cells in the module throughout the whole cycle at different T_{amb} and V_{in}. Due to the dynamic changing charge/discharge rates, the module mean temperature fluctuates significantly, but it is always kept between 20 °C and 40 °C, even when V_{in} reduces to 0.5 m s^{-1}, which is attributed to the using of 20 °C air-conditioned air. The red dash line represents the case where V_{in} = 0 m s^{-1} and only natural convection occurs. It indicates that the module will be overheated, leading to the risk of thermal runaway.

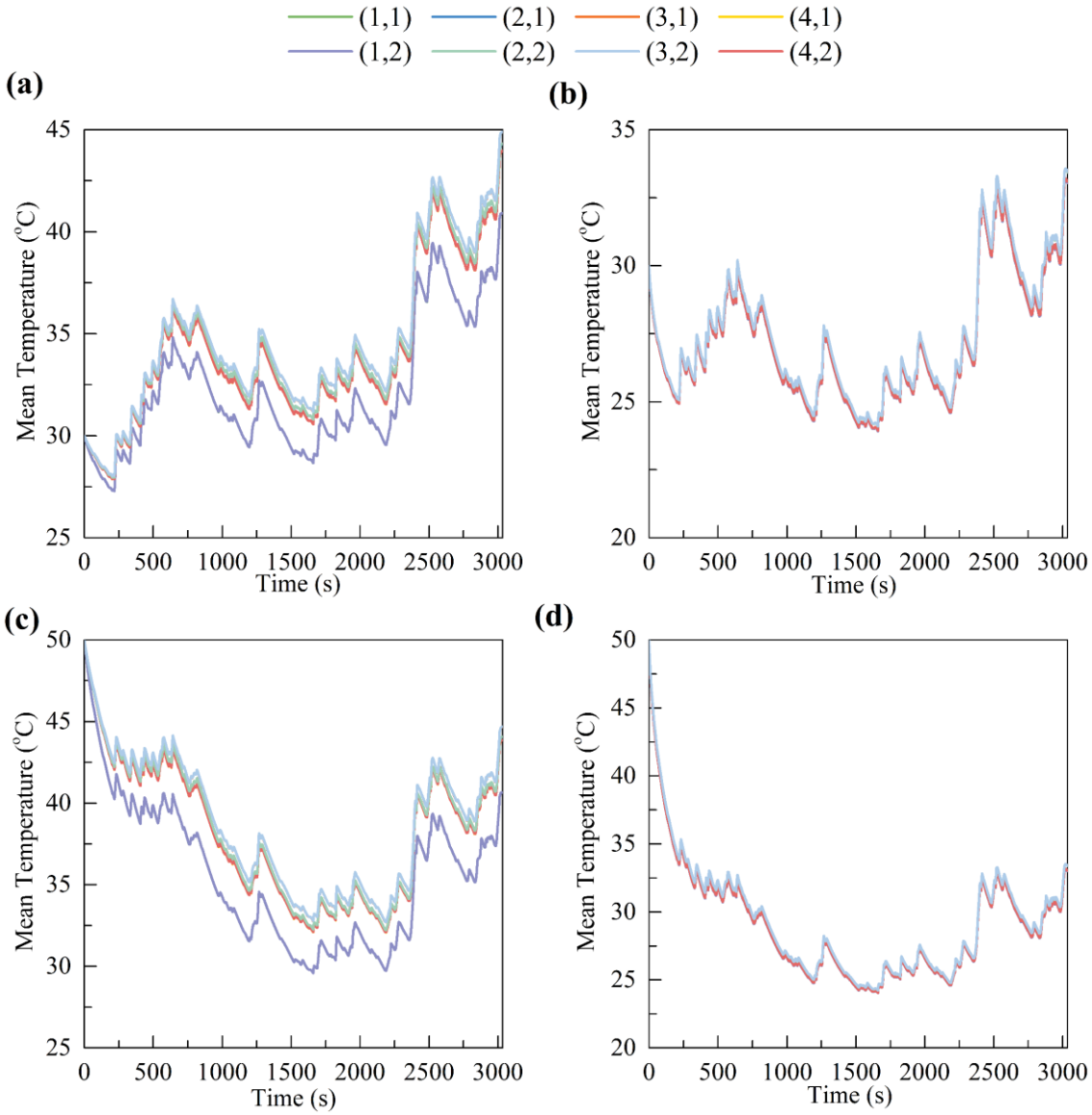

Fig. 9 Mean temperature curves of selected cells in the module: (a) T_{amb} = 30 °C, V_{in} = 0.5 m s^{-1}; (b) T_{amb} = 30 °C, V_{in} = 8 m s^{-1}; (c) T_{amb} = 50 °C, V_{in} = 0.5 m s^{-1}; and (d) T_{amb} = 50 °C, V_{in} = 8 m s^{-1}

Fig. 9 plots the mean temperature curves of different cells within the module in different conditions. The code of cells in the module is shown in Fig. 3. The maximum temperature difference between cells at V_{in} = 0.5 m s^{-1} is more than 2 °C in most of time, whereas the difference is minor at V_{in} = 8 m s^{-1}.

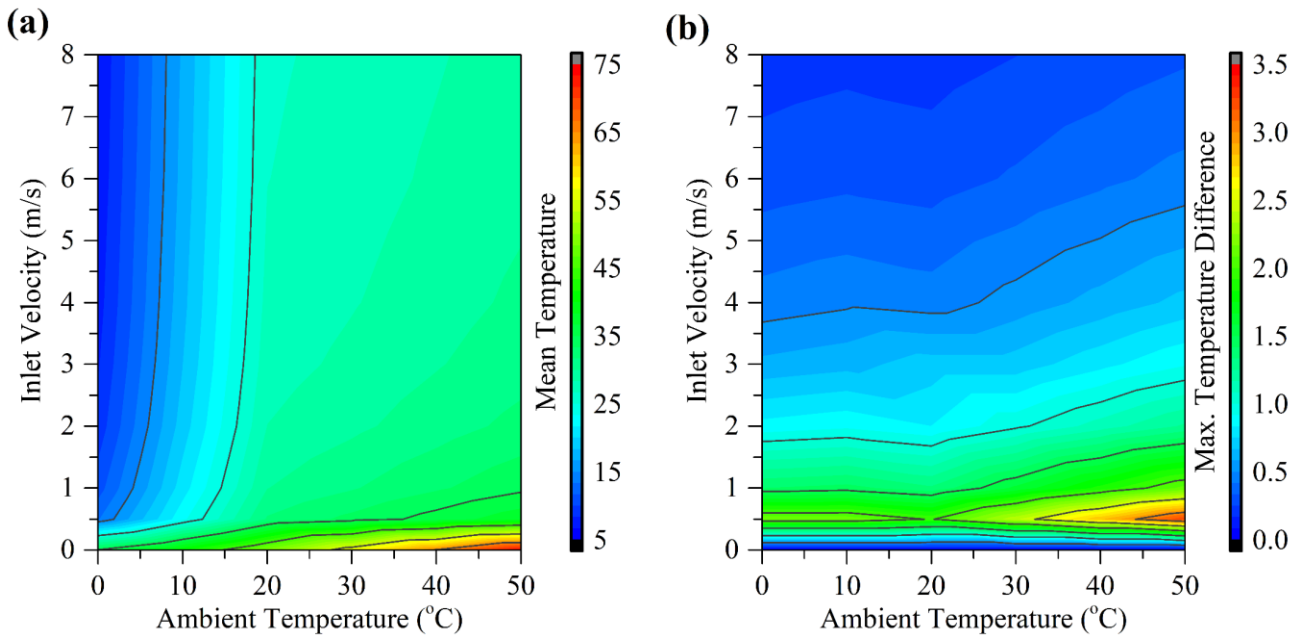

Fig. 10 Module temperature at different T_{amb} and V_{in}: (a) Mean temperature and (b) maximum temperature difference

Fig. 10(a) shows the time-averaged temperature of the module through the whole cycle decreases with the decrease of T_{amb} and the increase of V_{in}. There is little difference in temperature when V_{in} exceeds 0.5 m s^{-1}, indicating that the cooling efficiency is reduced.

Fig. 10(b) shows the maximum temperature difference (ΔT) between cells in the module. The maximum temperature difference (ΔT) is defined by:

$$\Delta T = \overline{T}_{\max} - \overline{T}_{\min} \tag{12}$$

where $\overline{T}_{max}$ and $\overline{T}_{min}$ are the maximum and minimum space and time-averaged cell temperature among the module, respectively. It can be seen that ΔT increases first and then decreases when V_{in} increases from 0 m s^{-1} to 8 m s^{-1}. The maximum ΔT is observed at T_{amb} = 50 °C and V_{in} = 0.5 m s^{-1}.

Fig. 11 shows the trajectories of capacity loss predicted by the degradation model [33]. The battery life is defined as the number of cycles that lead to a 20% capacity loss.

We use the mean cycle life ($\overline{N}$), maximum cycle life difference (ΔN) and maximum cycle life difference rate (ζ_N) to evaluate the degradation of the module, which are given by the following equations:

$$\overline{N} = \frac{\sum_{i=1}^{16} N_i}{16} \tag{13}$$

$$\Delta N = N_{\max} - N_{\min} \tag{14}$$

$$\zeta_N = \frac{\Delta N}{\bar{N}} \tag{15}$$

where N_i is the cycle life of each cell in the module, N_{max} and N_{min} are the maximum and minimum cycle life of the cell in the module.

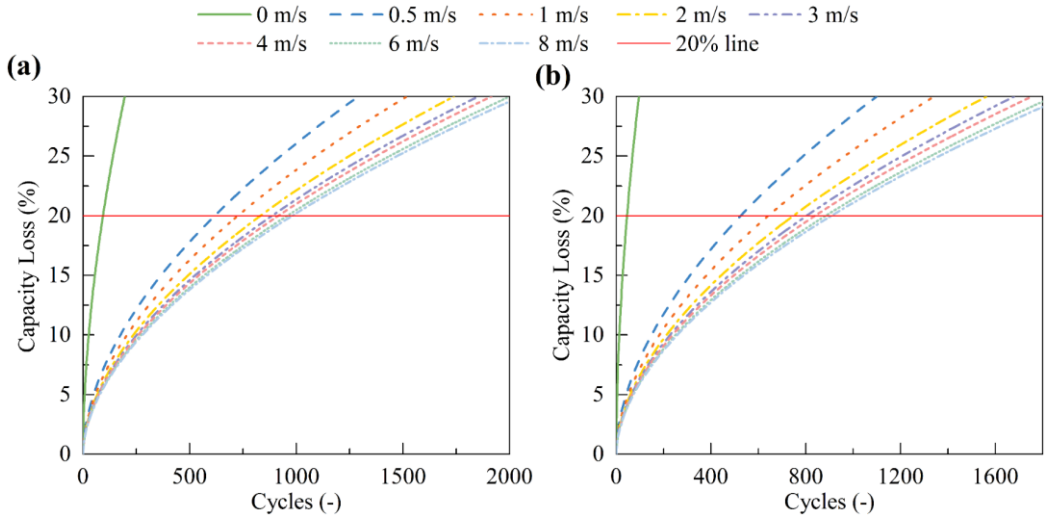

Fig. 11 Capacity loss trajectories: (a) T_{amb} = 30 °C and (b) T_{amb} =50°C.

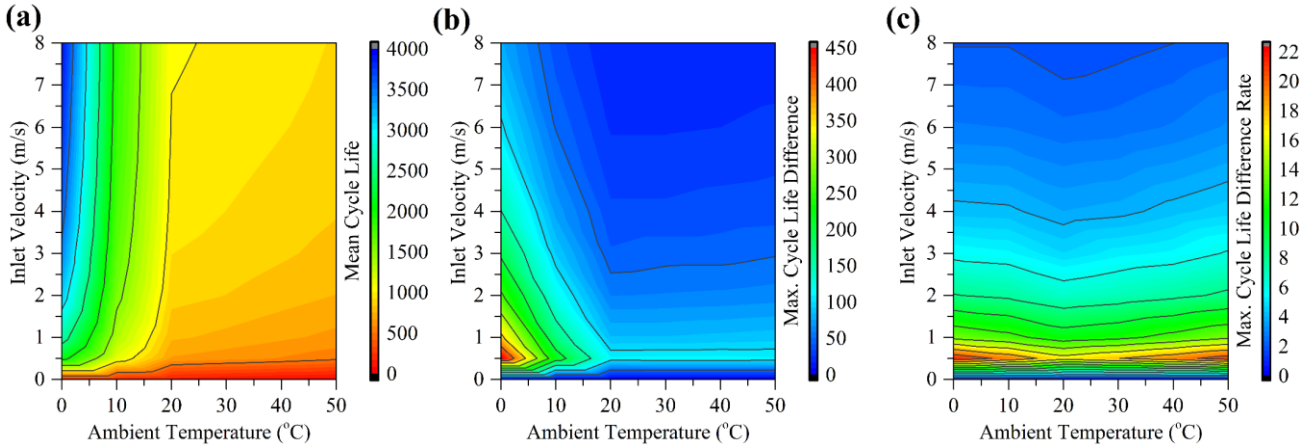

Fig. 12 Cycle life of the module at different T_{amb} and V_{in}: (a) Mean cycle life, (b) maximum cycle life difference and (c) maximum cycle life difference rate.

Fig. 12(a) illustrates $\bar{N}$ at different T_{amb} and V_{in}. Combining the results of Fig. 12(a) and Fig. 10, we can see that a high temperature leads to an enlarged capacity loss rate. Fig. 12(b) shows that ΔN is the highest at T_{amb} = 0 °C and V_{in} = 0.5 m s^{-1}, and it decreases with the increase of T_{amb} and V_{in}. Since the temperature distribution at V_{in} = 0 m s^{-1} is relatively uniform, ΔN is minor. However, ΔT is lowest at T_{amb} = 0 °C and it reaches the highest at T_{amb} = 50 °C, which shows the opposite trend with ΔN. This is because battery capacity loss and temperature follows an Arrhenius type relation, meaning that the degradation rate is more sensitive to temperature and little temperature difference will lead to large degradation non-uniformity in a cold environment. Fig. 13(a) demonstrates abovementioned rule by

plotting simulation results of ΔT and ΔN of this study. Results obtained at same T_{amb}, which also reflects different temperature levels of battery module, are plotted together.

Fig. 12(c) shows ζ_N varies little at different T_{amb} if V_{in} remains unchanged. As expected, with increased V_{in}, ζ_N shows a trend of increasing first and decreasing afterwards. The maximum ζ_N is observed at V_{in} = 0.5 m s^{-1} and it is higher than 20%. It should be noted that ζ_N at a low T_{amb} is not significantly larger than the other conditions due to prolonged cycle life, though its ΔT is the largest. Fig. 13(b) plots the relationships between ΔT and ζ_N at different T_{amb}. It shows that a small ΔT will lead to a large ζ_N at the low-temperature condition.

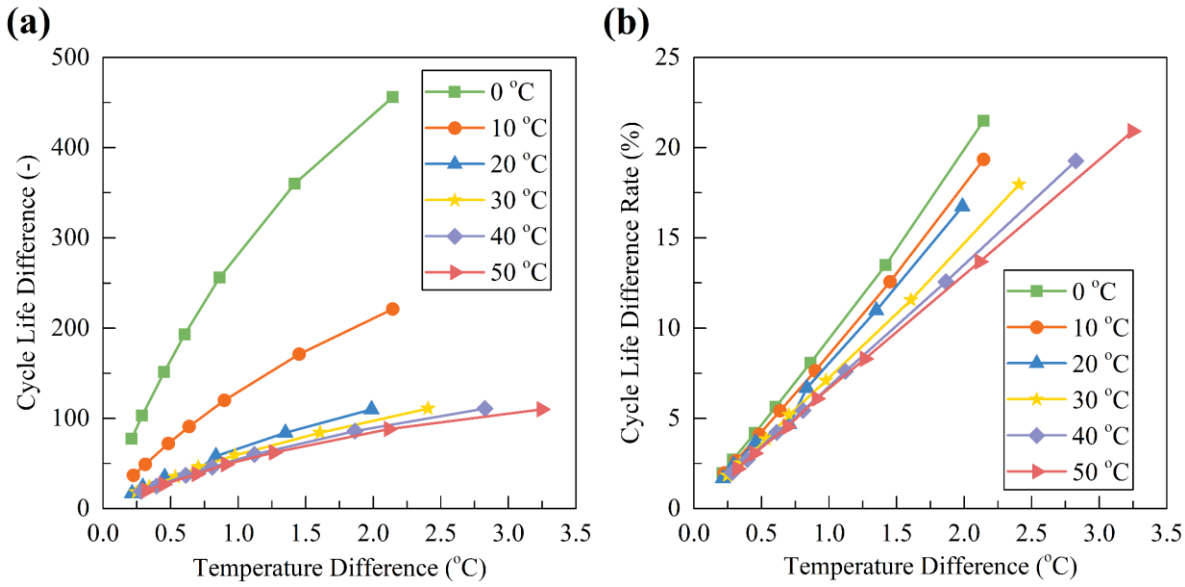

Fig. 13 Relationship between temperature difference and degradation non-uniformity at different temperatures: (a) Effects of ΔT to ΔN and (b) effects of ΔT to ζ_N.

4.2 PCM cooling

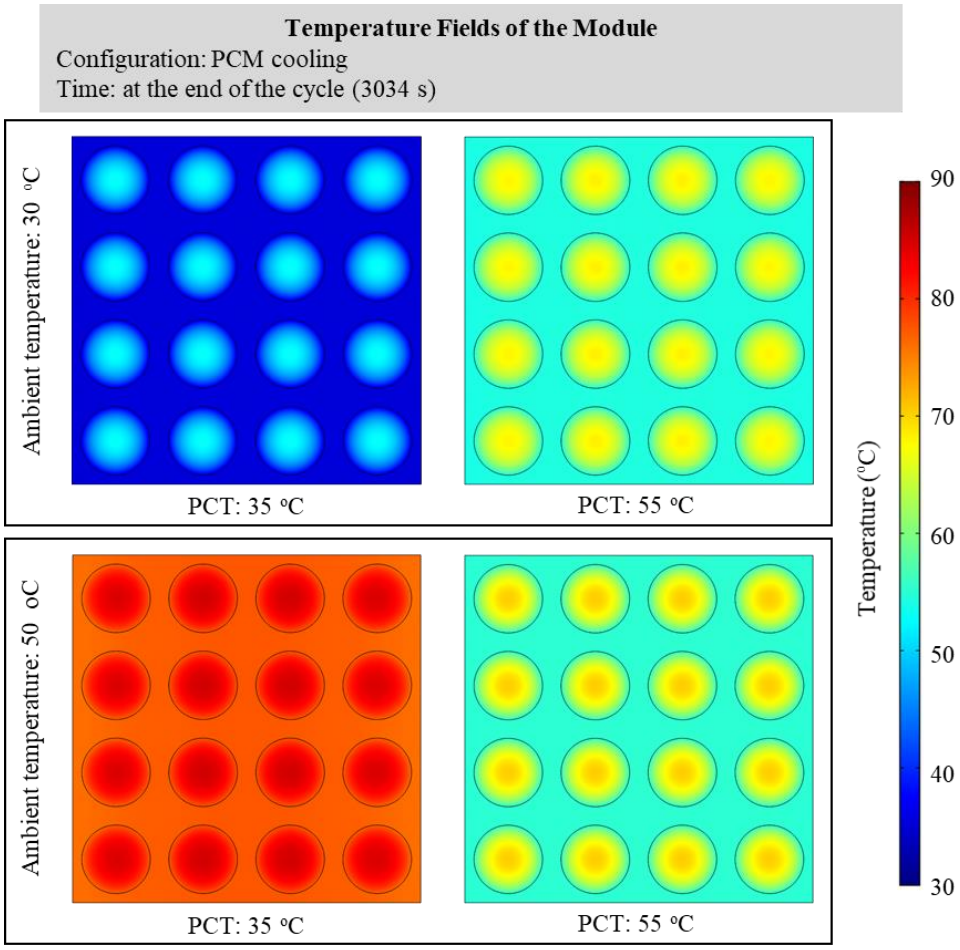

Fig. 14 Temperature fields of the module at the end of the driving cycle

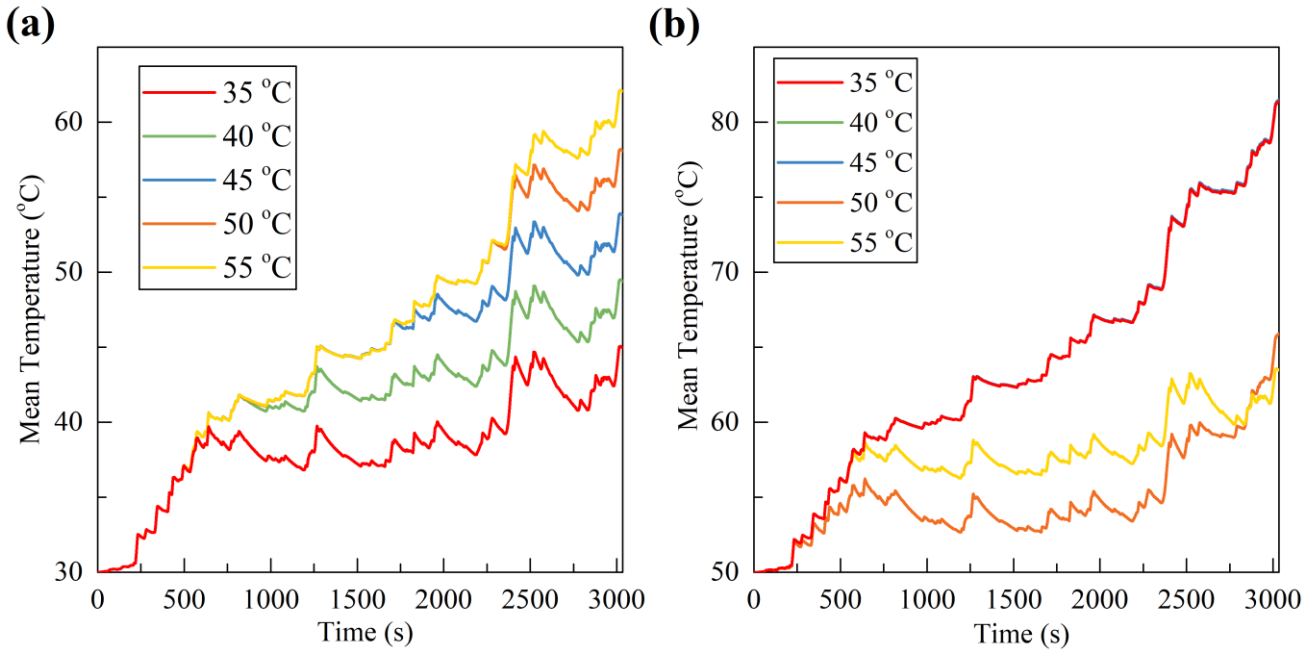

Fig. 15 Mean temperature curve of the module through the whole cycle at different PCT: (a) T_{amb} = 30 °C and (b) T_{amb} = 50 °C.

Fig. 14 and Fig. 15 show the temperature fields of the module at the end of the cycle and the mean

temperatures of all cells in the module throughout the whole cycle at different T_{amb} and PCT, respectively. Different from cases of air cooling, the module temperature keeps rising rather than fluctuates in a range. Mean temperature curves of selected cells in the module are shown in Appendix Fig. 11A.

Fig. 16(a) shows the time-averaged temperature of the module throughout the whole cycle. We can see the module mean temperature rises with the increase of T_{amb}. The PCM with a lower PCT has a better cooling effect at low T_{amb}. However, when T_{amb} reaches a certain value, the module mean temperature rises significantly. This is because PCM is completely melted before the end of cycle in these cases, which can be seen from the liquid phase fraction results shown in Fig. 17. Fig. 16(b) shows the ΔT is lower than 0.4 °C in all conditions, indicating PCM cooling can achieve much better uniformity than its air cooling counterpart. Meanwhile, a strong correlation between ΔT and liquid phase fraction can be found in Fig. 16(b) and Fig. 17. A higher liquid phase fraction leads to smaller ΔT before complete phase transition. But once the PCM has completely melted, ΔT will rise rapidly.

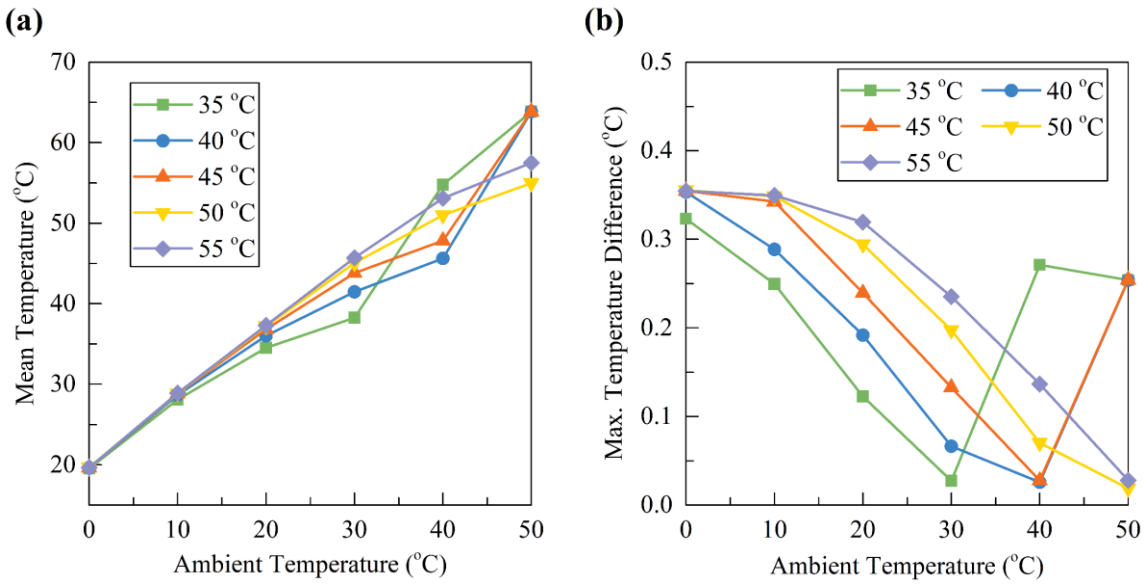

Fig. 16 Module temperature at different T_{amb} and PCTs: (a) Mean temperature and (b) max. temperature difference.

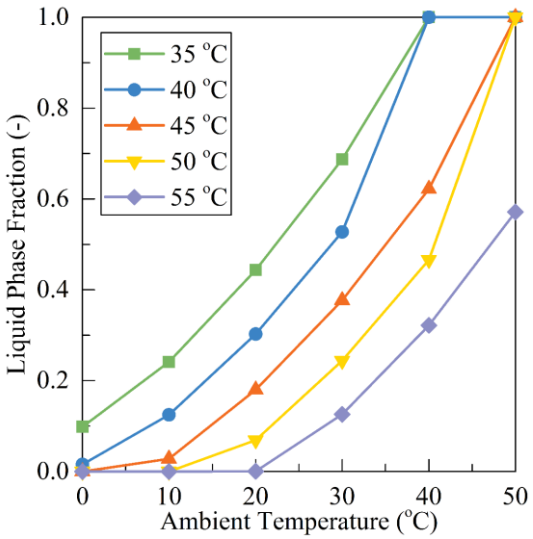

Fig. 17 Liquid phase fraction of PCM at the end of the cycle

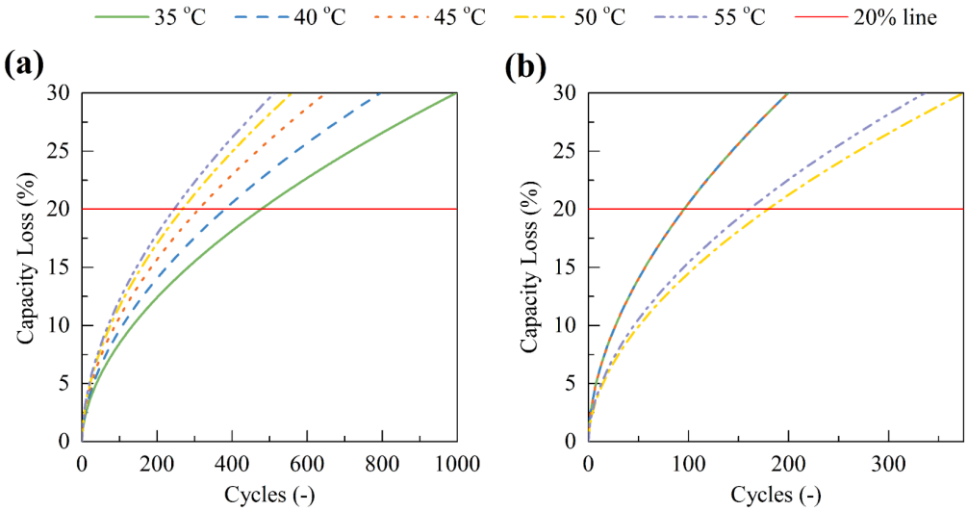

Fig. 18 Capacity loss trajectories: (a) T_{amb} =30 °C and (b) T_{amb} = 50 °C.

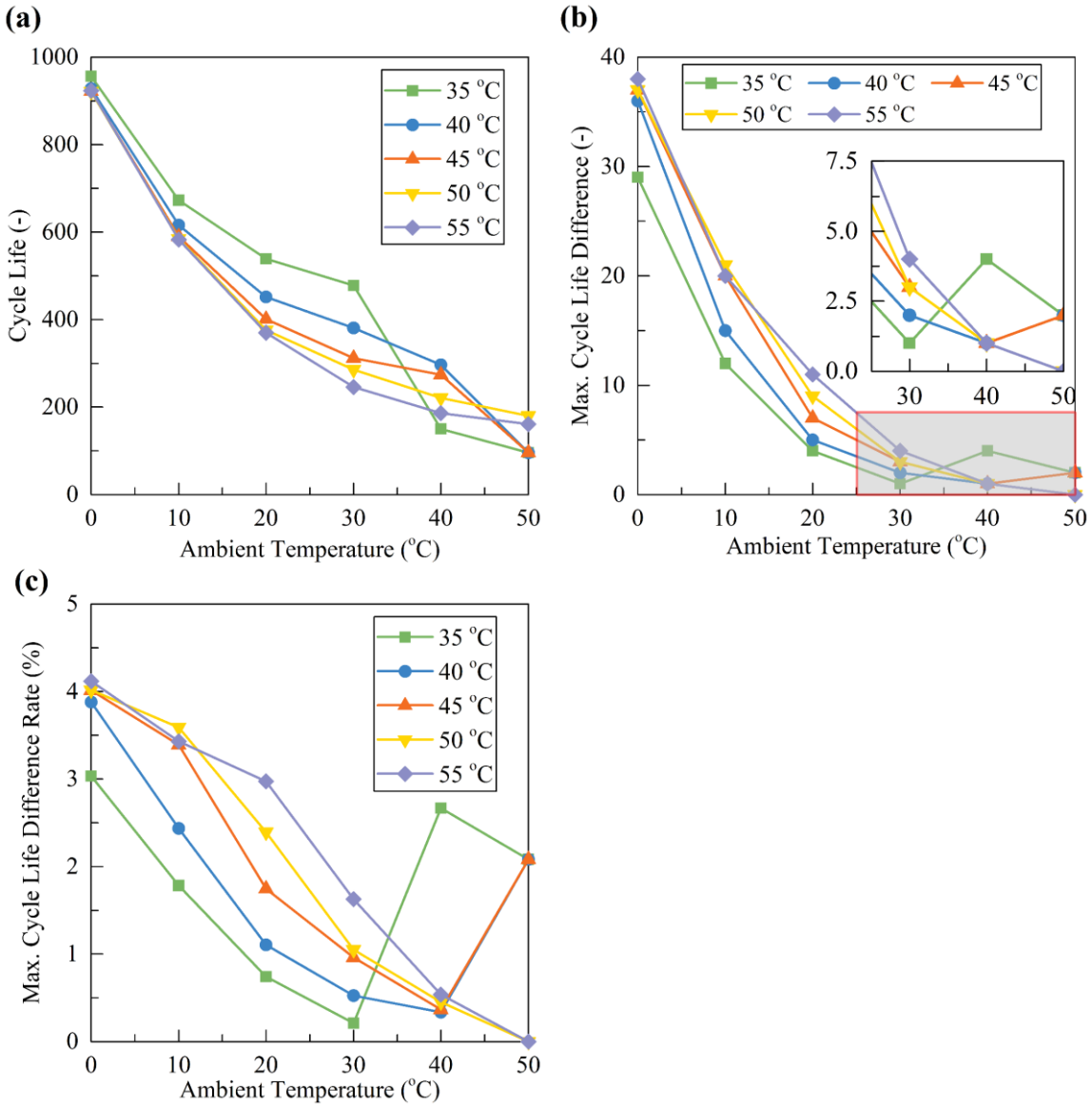

Fig. 19 Cycle life of the module at different T_{amb} and PCT: (a) Mean cycle life, (b) maximum cycle life difference and (c) maximum cycle life difference rate.

Fig. 18 and Fig. 19 show the capacity degradation trajectories of representative cases and cycle life of the module, respectively. Fig. 19(a) and Fig. 19(b) illustrate that when T_{amb} increases from 0 °C to 50 °C, the $\overline{N}$ drops from 900-1000 to less than 200, and ΔN reduces from 30-40 to less than 10. Fig. 19(c) shows the ζ_N is lower than 5% in all cases. It is the highest at T_{amb} = 0 °C and then decreases with the increase of T_{amb}. However, there are sharp rises at high T_{amb} in some cases. Fig. 19 also shows that the PCM with lower PCT can achieve improved cycle life. However, it is more likely to be completely melted in continuous charging/discharging cycle with high rates and at high T_{amb} conditions, which will put the battery module at the risk of accelerating the degradation process. In consequence, it's a conflict while choosing the type of PCM especially when the battery pack is to be used in a wide T_{amb}

range.

4.3 Comparison of air and PCM cooling strategies

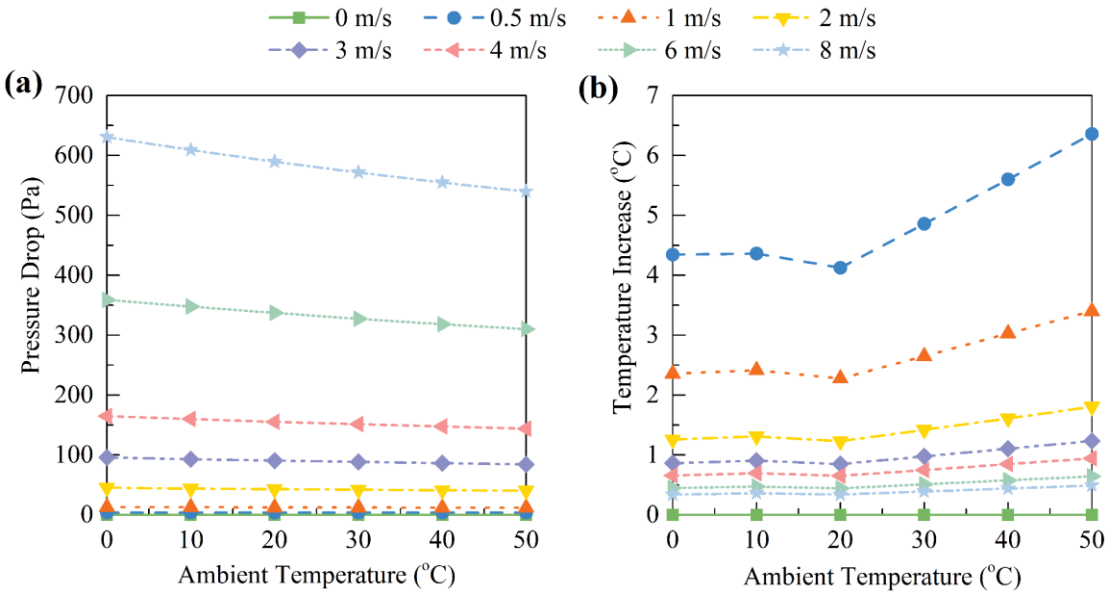

Fig. 20 Pressure drop (a) and temperature increase (b) between inlet and outlet of cooling air

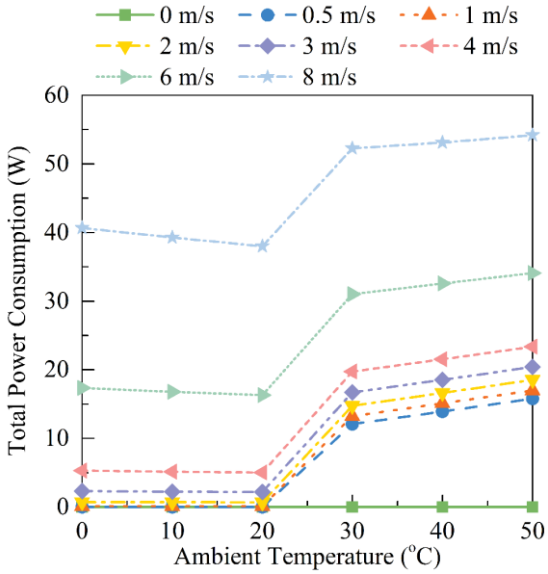

Fig. 21 Total power consumption of air cooling

In this section, the performance of air cooling and PCM cooling are compared with respect to their power consumption and battery cycle life.

Because PCM cooling is a passive BTMS and does not consume energy, we emphasize on the energy consumption analysis of air cooling. Power consumption considered in this study includes the pumping power of the fan and refrigerating power of the air conditioning system. The ideal pumping power consumption is calculated using Eq.(16):

$$P_{fan} = \Delta p \cdot \dot{V} \tag{16}$$

where Δp is the pressure drop from the inlet to the outlet of duct; $\dot{V}$ is the volume flow rate of cooling air.

The refrigerating power is evaluated by assuming that the refrigeration cycle of the air conditioning system has a constant Coefficient of Performance (COP) of 2 in all conditions [42]. Thus, the ideal refrigerating power consumption can be calculated by Eq.(17) :

$$P_{AC} = \dot{m}_{air} C_{p,air} \Delta T_{air} / COP \tag{17}$$

where $\dot{m}_{air}$ is the mass flow rate; ΔT_{air} is the temperature increase of the cooling air from the inlet to the outlet.

Fig. 20 presents the pressure drop and temperature increase between the inlet and the outlet of cooling air. Fig. 21 shows the ideal power consumptions of fan and air conditioning system. A sharp rise of power consumption while increasing V_{in} can be observed, which is attributed to the dramatically rising fan power. Total power consumption also increases when T_{amb} rises to 30 °C because the air-conditioning system is turned on to produce 20 °C cooling air.

To evaluate the cost performance of air cooling and PCM cooling systems, this study take battery cycle life as an additional performance indicator of BTMS on top of battery maximum temperature, temperature non-uniformity and power consumption which are taken as the main performance indicators in most previous studies and an evaluation index of cyclical cost (δ) is proposed to link indicators of power consumption and battery cycle life together. δ is defined as the ratio of the total cost, including purchasing cost of the battery module and parasitic energy cost of BTMS to the module cycle life (capacity loss reaches 20%). δ is expressed as the following equation:

$$\delta = \frac{\tau_{batt} \cdot C_{nom}^{PACK} + \beta \cdot N_{eof} \cdot Q_p}{N_{eof}} \tag{18}$$

$$\beta = \frac{\tau_f}{H_{fuel} \eta_{PT}} \tag{19}$$

where τ_{batt} is the battery; C_{nom}^{PACK} is the nominal capacity of the battery module; N_{eof} is the number of cycles of the battery pack before end of life; Q_p is the parasitic energy consumption per cycle; τ_f is the fuel price; H_{fuel} is the lower heating value of the fuel; η_{PT} is efficiency of the hybrid powertrain and is assumed to be 30.1% [43]. Table 7 lists the values of Q_p, τ_f and H_{fuel} obtained from Ref. [44]. Such economic index is also a common practice in the researches of power management for HEV [37,44–46].

Table 7: Main parameters for cost evaluation[44]

parameter	Value
battery price [€ kWh^{-1}]	900
Fuel price [€ L^{-1}]	1.34
Diesel lower heating value [MJ L^{-1}]	38.6

Cases of air cooling at V_{in} = 0.5 m s^{-1}, PCM cooling at PCT = 45 °C and no BTMS are chosen for comparison. Fig. 22(a) presents the $\overline{N}$, N_{max} and N_{min} of three conditions. It shows air cooling can achieve the highest cycle life and the largest non-uniformity. Fig. 22(b) shows δ of the battery module can be reduced by using active air and passive PCM cooling. Besides, air cooling has at least 50% lower δ than that of PCM cooling though it has parasitic power consumption. δ of the PCM cooling is also more sensitive to the T_{amb}, especially when T_{amb} exceeds the PCT of the PCM. Fig. 23 shows δ in air cooling condition at different T_{amb} and V_{in}. δ of battery module first decreases and then increases with the increase of V_{in}, and there are optimal V_{in} for the lowest δ at different T_{amb}.

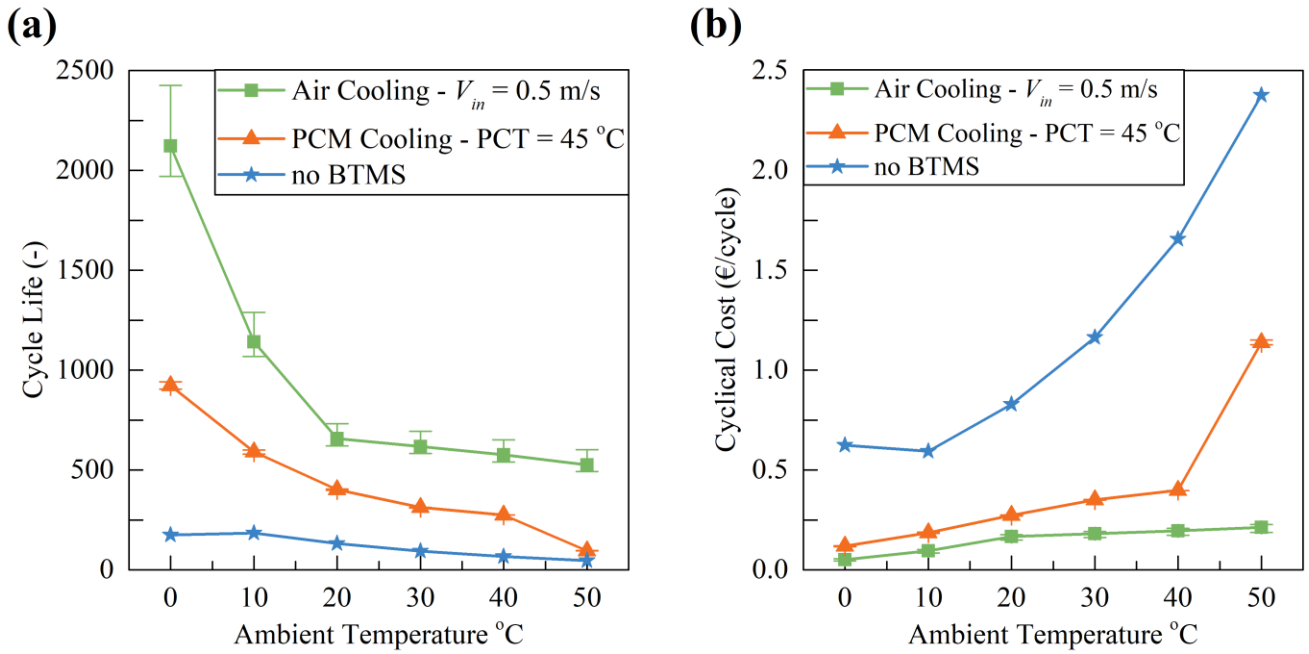

Fig. 22 Cycle life (a) and cyclical cost (b) comparison of air cooling (V_{in} = 0.5 m s^{-1}), PCM cooling (PCT = 45 °C) and no BTMS

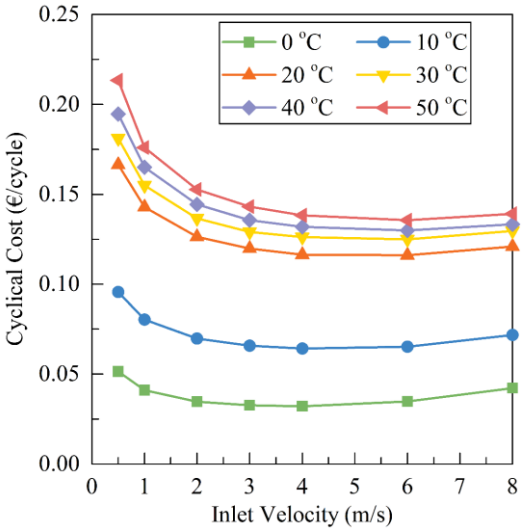

Fig. 23 Cyclical costs in air cooling condition at different T_{amb} and V_{in}

5. Conclusions

This study analyses the thermal states and cycle life of a battery module under a dynamic current load obtained from a hybrid electric bus (16.55 km in approximately 3000 s) when active air cooling using air-conditioned air and passive PCM cooling are independently applied for thermal management. The effects of inlet velocity (V_{in}), PCM phase change temperature (PCT) and ambient temperature (T_{amb}) are studied. The following are conclusions drawn from results and discussion.

1. Active air cooling using air-conditioned air is able to keep the module temperature under safety range even at T_{amb} as high as 50 °C, whereas passive PCM based BTMS in which PCM is cooled by natural convection with air at ambient temperature is difficult to achieve this. However, a more uniform temperature field can be obtained with PCM cooling.

2. Due to the lower temperature field in air cooling condition, module cycle life is extended by up to 600% compared with that of the PCM cooling. In the air cooling condition, the maximum cycle life difference rate (ζ_N) is over 20% at a low V_{in}, e.g. 0.5 m s^{-1}. With the increase of V_{in}, ζ_N is reduced. In PCM cooling condition, ζ_N is lower than 5% and the largest value is 4.1%, which has a strong link to the liquid phase fraction of PCM.

3. The cyclical cost (δ) of the battery module using air-conditioned air cooling is much lower than that using PCM cooling. In PCM cooling, δ can be double due to limited module cycle life. For the air cooling, the δ first decreases and then increases while increasing V_{in}. There exists an optimal V_{in} for the lowest δ at different T_{amb}.

4. To extend the life and reduce operating cost of LIBs by means of thermal management, active air cooling is the better choice than passive PCM only cooling. For the purpose of both extending the life

and improving the uniformity of the LIB pack, PCM and active compound system may be the best choice.

Acknowledgements

The authors highly acknowledge the finical support from Science and Technology Planned Project of Zhejiang Province (No. 2018C01057).

Reference

[1] M.Z. Jacobson, Review of solutions to global warming, air pollution, and energy security, Energy Environ. Sci. 2 (2009) 148–173.

[2] A. Barré, B. Deguilhem, S. Grolleau, M. Gérard, F. Suard, D. Riu, A review on lithium-ion battery ageing mechanisms and estimations for automotive applications, J. Power Sources. 241 (2013) 680–689.

[3] M.M. Thackeray, C. Wolverton, E.D. Isaacs, Electrical energy storage for transportation - Approaching the limits of, and going beyond, lithium-ion batteries, Energy Environ. Sci. 5 (2012) 7854–7863.

[4] G. Zubi, R. Dufo-López, M. Carvalho, G. Pasaoglu, The lithium-ion battery: State of the art and future perspectives, Renew. Sustain. Energy Rev. 89 (2018) 292–308.

[5] W. Lv, Z. Wang, H. Cao, Y. Sun, Y. Zhang, Z. Sun, A Critical Review and Analysis on the Recycling of Spent Lithium-Ion Batteries, ACS Sustain. Chem. Eng. 6 (2018) 1504–1521.

[6] K. Zhao, L. Zhang, R. Xia, Y. Dong, W. Xu, C. Niu, L. He, M. Yan, L. Qu, L. Mai, SnO2 Quantum Dots@Graphene Oxide as a High-Rate and Long-Life Anode Material for Lithium-Ion Batteries, Small. 12 (2016) 588–594.

[7] W. Liu, X. Li, D. Xiong, Y. Hao, J. Li, H. Kou, B. Yan, D. Li, S. Lu, A. Koo, K. Adair, X. Sun, Significantly improving cycling performance of cathodes in lithium ion batteries: The effect of Al 2 O 3 and LiAlO 2 coatings on LiNi 0.6 Co 0.2 Mn 0.2 O 2, Nano Energy. 44 (2018) 111–120.

[8] W. Gao, Y. Zheng, M. Ouyang, J. Li, X. Lai, X. Hu, Micro-short-circuit diagnosis for series-connected lithium-ion battery packs using mean-difference model, IEEE Trans. Ind. Electron. 66 (2019) 2132–2142.

[9] B. Xia, Y. Shang, T. Nguyen, C. Mi, A correlation based fault detection method for short circuits in battery packs, J. Power Sources. 337 (2017) 1–10.

[10] J. Wei, G. Dong, Z. Chen, Y. Kang, System state estimation and optimal energy control framework for multicell lithium-ion battery system, Appl. Energy. 187 (2017) 37–49.

[11] M.M. Hoque, M.A. Hannan, A. Mohamed, A. Ayob, Battery charge equalization controller in electric vehicle applications: A review, Renew. Sustain. Energy Rev. 75 (2017) 1363–1385.

[12] L.H. Saw, Y. Ye, A.A.O. Tay, W.T. Chong, S.H. Kuan, M.C. Yew, Computational fluid dynamic and thermal analysis of Lithium-ion battery pack with air cooling, Appl. Energy. 177 (2016) 783–792.

[13] E. Jiaqiang, D. Han, A. Qiu, H. Zhu, Y. Deng, J. Chen, X. Zhao, W. Zuo, H. Wang, J. Chen, Q. Peng, Orthogonal experimental design of liquid-cooling structure on the cooling effect of a liquid-cooled battery thermal management system, Appl. Therm. Eng. 132 (2018) 508–520.

[14] D. Zou, X. Ma, X. Liu, P. Zheng, Y. Hu, Thermal performance enhancement of composite phase change materials (PCM) using graphene and carbon nanotubes as additives for the potential application in lithium-ion power battery, Int. J. Heat Mass Transf. 120 (2018) 33–41.

[15] Y. Ye, Y. Shi, L.H. Saw, A.A.O. Tay, Performance assessment and optimization of a heat pipe thermal management system for fast charging lithium ion battery packs, Int. J. Heat Mass Transf. 92 (2016) 893–903.

[16] J. Zhao, P. Lv, Z. Rao, Experimental study on the thermal management performance of phase change material coupled with heat pipe for cylindrical power battery pack, Exp. Therm. Fluid Sci. 82 (2017) 182–188.

[17] M. Al-Zareer, I. Dincer, M.A. Rosen, Novel thermal management system using boiling cooling for high-powered lithium-ion battery packs for hybrid electric vehicles, J. Power

Sources. 363 (2017) 291–303.
[18] A.M. Sefidan, A. Sojoudi, S.C. Saha, Nanofluid-based cooling of cylindrical lithium-ion battery packs employing forced air flow, Int. J. Therm. Sci. 117 (2017) 44–58.
[19] J. Wang, J. Purewal, P. Liu, J. Hicks-Garner, S. Soukazian, E. Sherman, A. Sorenson, L. Vu, H. Tataria, M.W. Verbrugge, Degradation of lithium ion batteries employing graphite negatives and nickel-cobalt-manganese oxide + spinel manganese oxide positives: Part 1, aging mechanisms and life estimation, J. Power Sources. 269 (2014) 937–948.
[20] J. Neubauer, E. Wood, Thru-life impacts of driver aggression, climate, cabin thermal management, and battery thermal management on battery electric vehicle utility, J. Power Sources. 259 (2014) 262–275.
[21] T. Yuksel, S. Litster, V. Viswanathan, J.J. Michalek, Plug-in hybrid electric vehicle LiFePO 4 battery life implications of thermal management, driving conditions, and regional climate, J. Power Sources. 338 (2017) 49–64.
[22] M. Doyle, Modeling of Galvanostatic Charge and Discharge of the Lithium/Polymer/Insertion Cell, J. Electrochem. Soc. 140 (1993) 1526.
[23] T.F. Fuller, Simulation and Optimization of the Dual Lithium Ion Insertion Cell, J. Electrochem. Soc. 141 (1994) 1.
[24] P. Amiribavandpour, W. Shen, D. Mu, A. Kapoor, An improved theoretical electrochemical-thermal modelling of lithium-ion battery packs in electric vehicles, J. Power Sources. 284 (2015) 328–338.
[25] E. Prada, D. Di Domenico, Y. Creff, J. Bernard, V. Sauvant-Moynot, F. Huet, Simplified Electrochemical and Thermal Model of LiFePO $_4$ -Graphite Li-Ion Batteries for Fast Charge Applications, J. Electrochem. Soc. 159 (2012) A1508–A1519.
[26] Y. Ye, Y. Shi, A.A.O. Tay, Electro-thermal cycle life model for lithium iron phosphate battery, J. Power Sources. 217 (2012) 509–518.
[27] J. Voelcker, Lithium batteries take to the road, IEEE Spectr. 44 (2007) 26–31.
[28] M. Safari, C. Delacourt, Modeling of a commercial graphite/LiFePO4 cell, J. Electrochem. Soc. 158 (2011) 562–571.
[29] J.L. Dodd, Phase composition and dynamical studies of lithium iron phosphate, 2007. http://thesis.library.caltech.edu/1662/.
[30] Y. Reynier, R. Yazami, B. Fultz, The entropy and enthalpy of lithium intercalation into graphite, J. Power Sources. 119–121 (2003) 850–855.
[31] Y. Li, Y. Du, T. Xu, H. Wu, X. Zhou, Z. Ling, Z. Zhang, Optimization of thermal management system for Li-ion batteries using phase change material, Appl. Therm. Eng. 131 (2018) 766–778.
[32] N. Javani, I. Dincer, G.F. Naterer, B.S. Yilbas, Heat transfer and thermal management with PCMs in a Li-ion battery cell for electric vehicles, Int. J. Heat Mass Transf. 72 (2014) 690–703.
[33] J. Wang, P. Liu, J. Hicks-Garner, E. Sherman, S. Soukiazian, M. Verbrugge, H. Tataria, J. Musser, P. Finamore, Cycle-life model for graphite-LiFePO4 cells, J. Power Sources. 196 (2011) 3942–3948.
[34] K. Shah, A. Jain, Prediction of thermal runaway and thermal management requirements in cylindrical Li-ion cells in realistic scenarios, Int. J. Energy Res. 43 (2019) 1827–1838.
[35] J. Zhao, Z. Rao, Y. Huo, X. Liu, Y. Li, Thermal management of cylindrical power battery module for extending the life of new energy electric vehicles, Appl. Therm. Eng. 85 (2015) 33–43.

[36] Z. Rao, Q. Wang, C. Huang, Investigation of the thermal performance of phase change material/mini-channel coupled battery thermal management system, Appl. Energy. 164 (2016) 659–669.
[37] X. Hu, L. Johannesson, N. Murgovski, B. Egardt, Longevity-conscious dimensioning and power management of the hybrid energy storage system in a fuel cell hybrid electric bus, Appl. Energy. 137 (2015) 913–924.
[38] F. He, H. Wang, L. Ma, Experimental demonstration of active thermal control of a battery module consisting of multiple Li-ion cells, Int. J. Heat Mass Transf. 91 (2015) 630–639.
[39] R. Sabbah, R. Kizilel, J.R. Selman, S. Al-Hallaj, Active (air-cooled) vs. passive (phase change material) thermal management of high power lithium-ion packs: Limitation of temperature rise and uniformity of temperature distribution, J. Power Sources. 182 (2008) 630–638.
[40] J. Jaguemont, N. Omar, P. Van den Bossche, J. Mierlo, Phase-change materials (PCM) for automotive applications: A review, Appl. Therm. Eng. 132 (2018) 308–320.
[41] T. ur Rehman, H.M. Ali, M.M. Janjua, U. Sajjad, W.M. Yan, A critical review on heat transfer augmentation of phase change materials embedded with porous materials/foams, Int. J. Heat Mass Transf. 135 (2019) 649–673.
[42] M. Shams-Zahraei, A.Z. Kouzani, S. Kutter, B. Bäker, Integrated thermal and energy management of plug-in hybrid electric vehicles, J. Power Sources. 216 (2012) 237–248.
[43] J. Thomas, Drive Cycle Powertrain Efficiencies and Trends Derived from EPA Vehicle Dynamometer Results, SAE Int. J. Passeng. Cars - Mech. Syst. 7 (2014) 1374–1384.
[44] X. Hu, N. Murgovski, L.M. Johannesson, B. Egardt, Comparison of three electrochemical energy buffers applied to a hybrid bus powertrain with simultaneous optimal sizing and energy management, IEEE Trans. Intell. Transp. Syst. 15 (2014) 1193–1205.
[45] S.J. Moura, H.K. Fathy, D.S. Callaway, J.L. Stein, A stochastic optimal control approach for power management in plug-in hybrid electric vehicles, IEEE Trans. Control Syst. Technol. 19 (2011) 545–555.
[46] S. Zhang, R. Xiong, F. Sun, Model predictive control for power management in a plug-in hybrid electric vehicle with a hybrid energy storage system, Appl. Energy. 185 (2017) 1654–1662.

Appendix

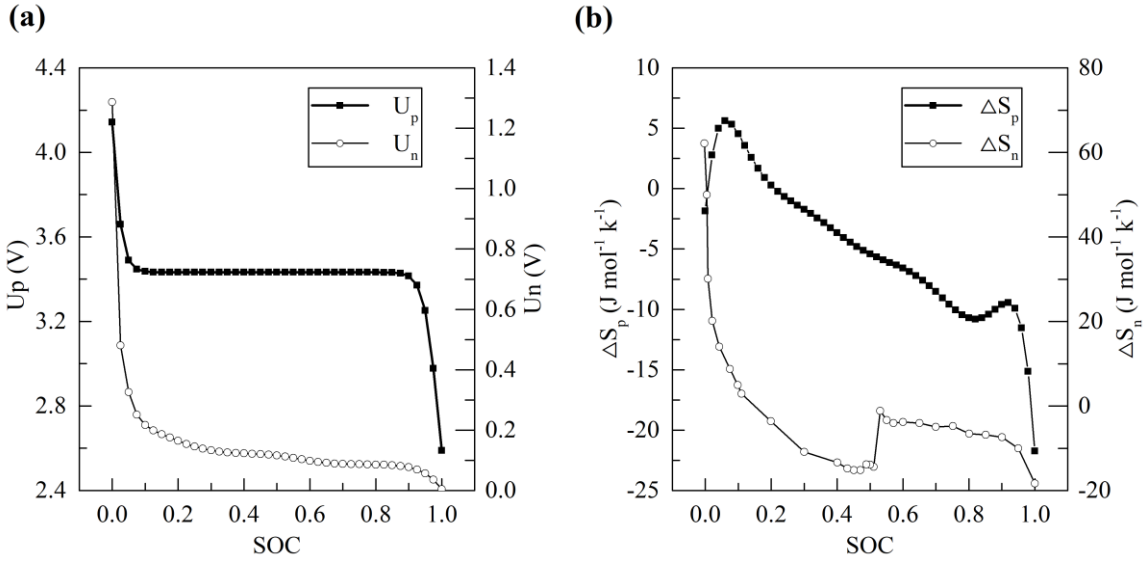

Fig. 1A Reference open circuit potential (a) and entropy change (b)

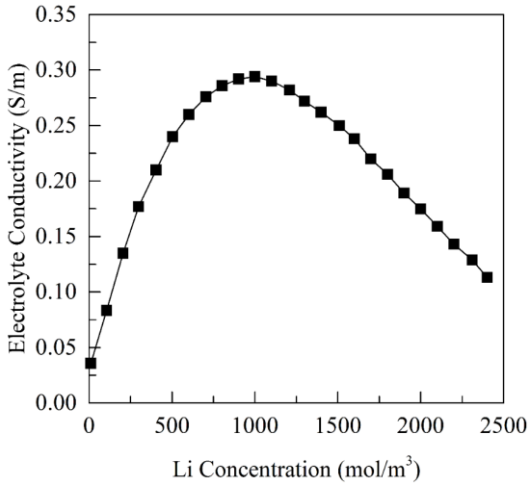

Fig. 2A Electrolyte conductivity as a function of Li concentration

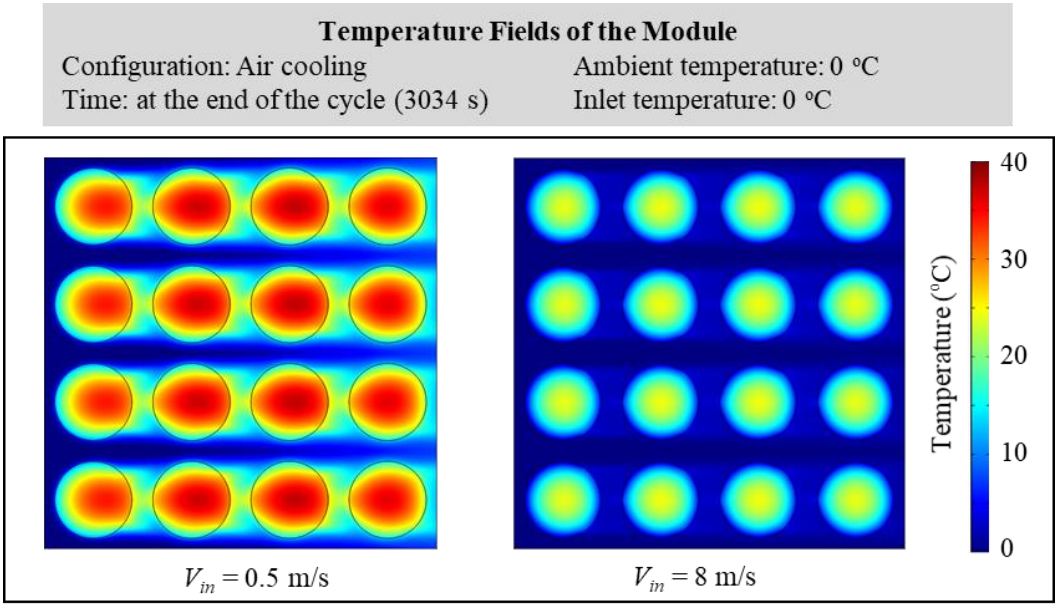

Fig. 3A Temperature fields of the module at the end of the driving cycle of air cooling at T_{amb} = 0 °C

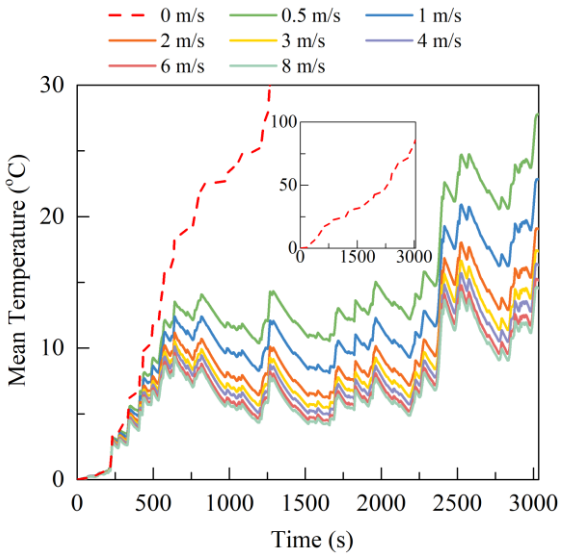

Fig. 4A Module mean temperature curves through the whole cycle of air cooling at T_{amb}=0 °C

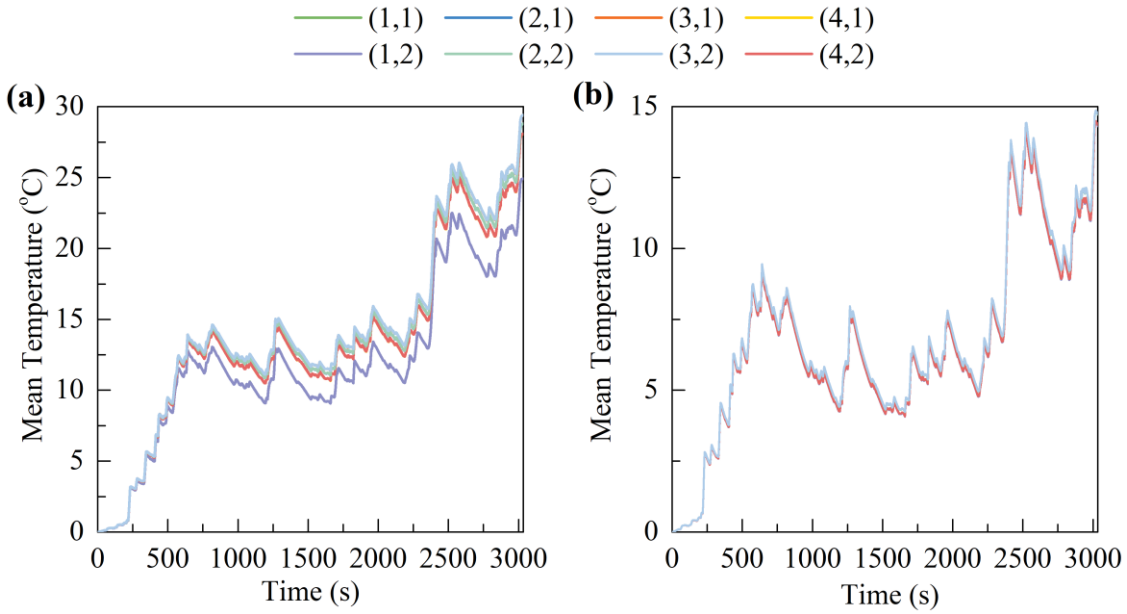

Fig. 5A Mean temperature curves of selected cells in the module of air cooling at T_{amb}=0 °C: (a) V_{in} = 0.5 m s^{-1} and (b) V_{in} = 8 m s^{-1}

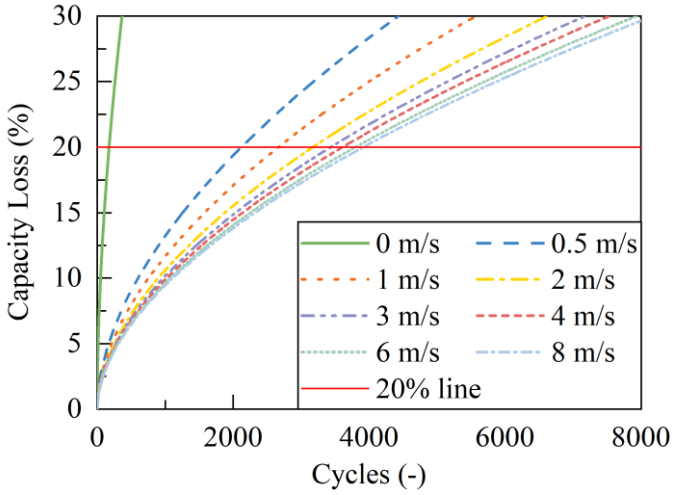

Fig. 6A Capacity loss trajectories of air cooling at T_{amb}=0 °C

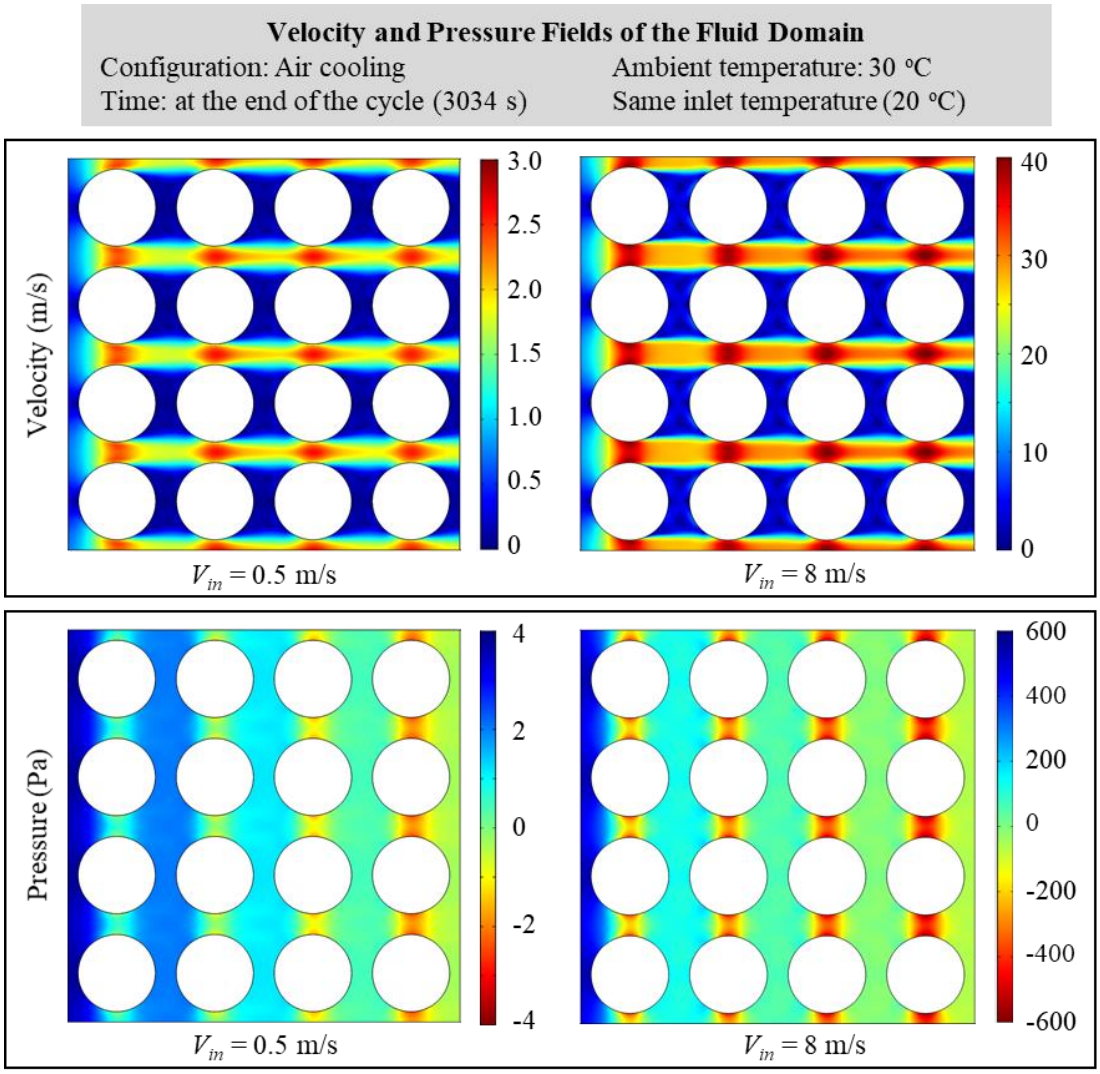

Fig. 7A Velocity and pressure fields of the fluid domain of air cooling at T_{amb} = 30 °C

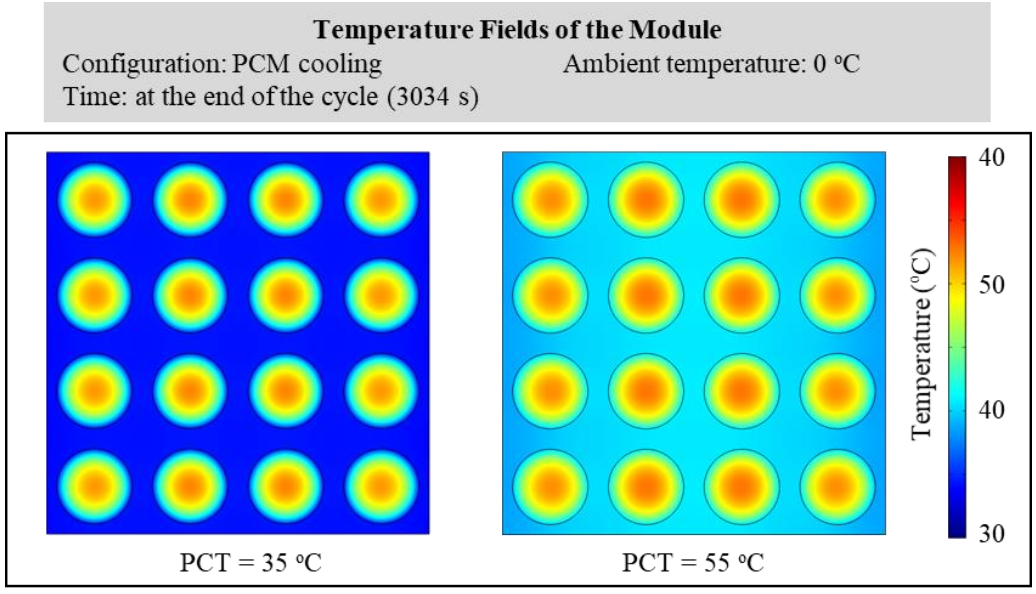

Fig. 8A Temperature fields of the module at the end of the driving cycle of PCM cooling at T_{amb} = 0 °C

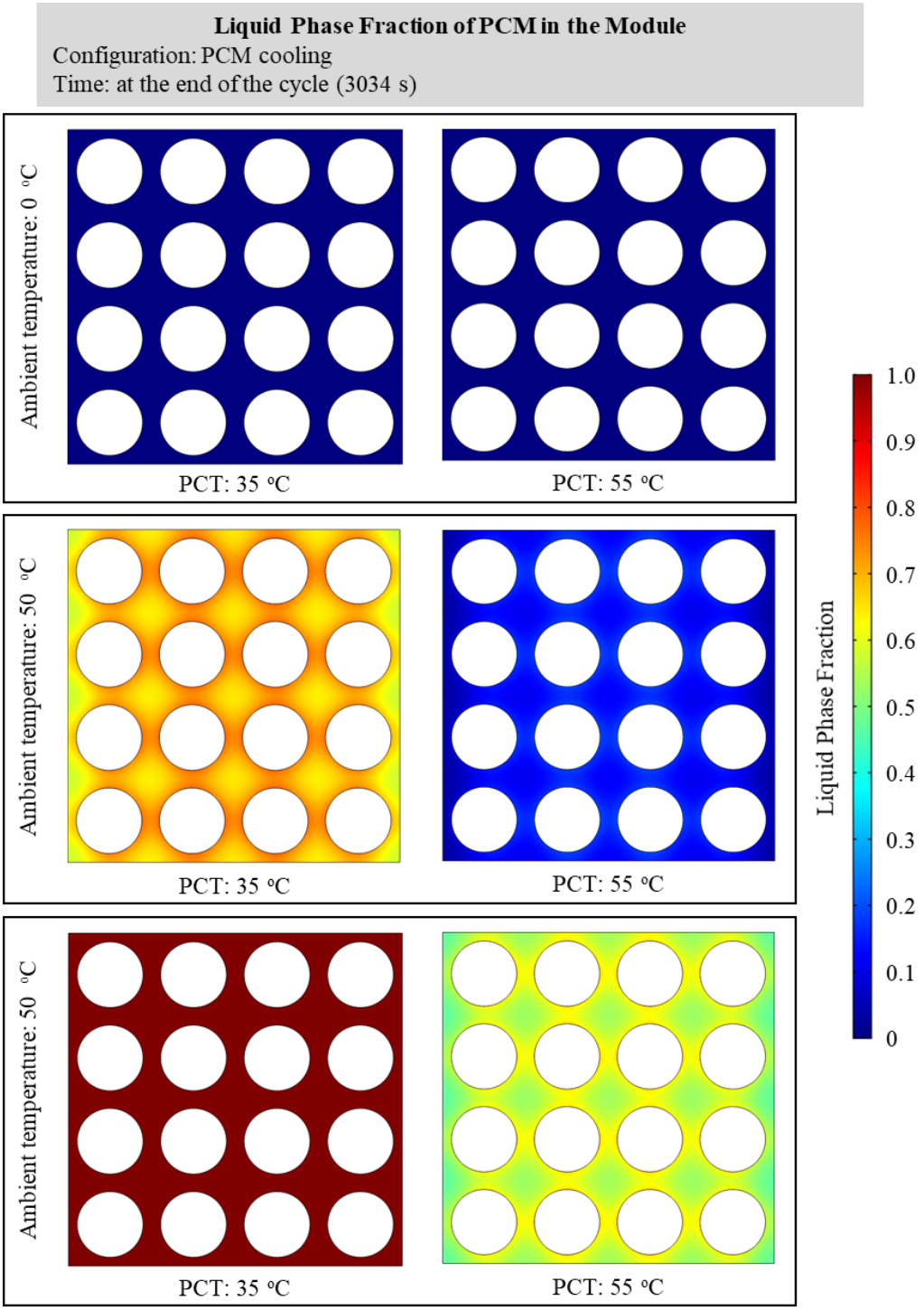

Fig. 9A Liquid phase fraction of PCM in the module at the end of driving cycle

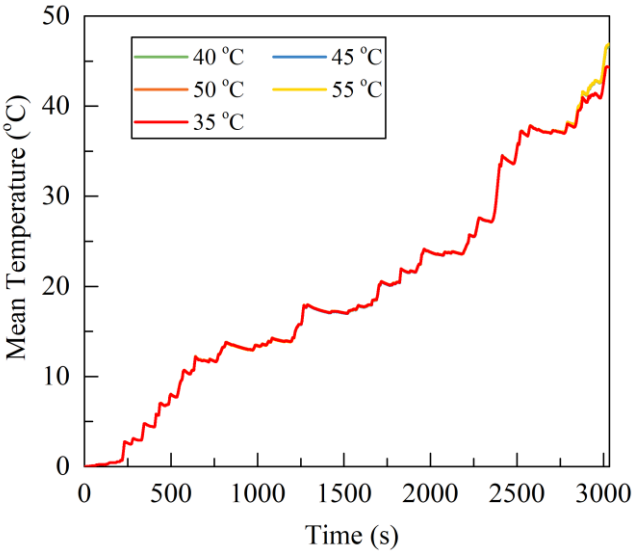

Fig. 10A Mean temperature curves of the module of PCM cooling at T_{amb}=0 °C

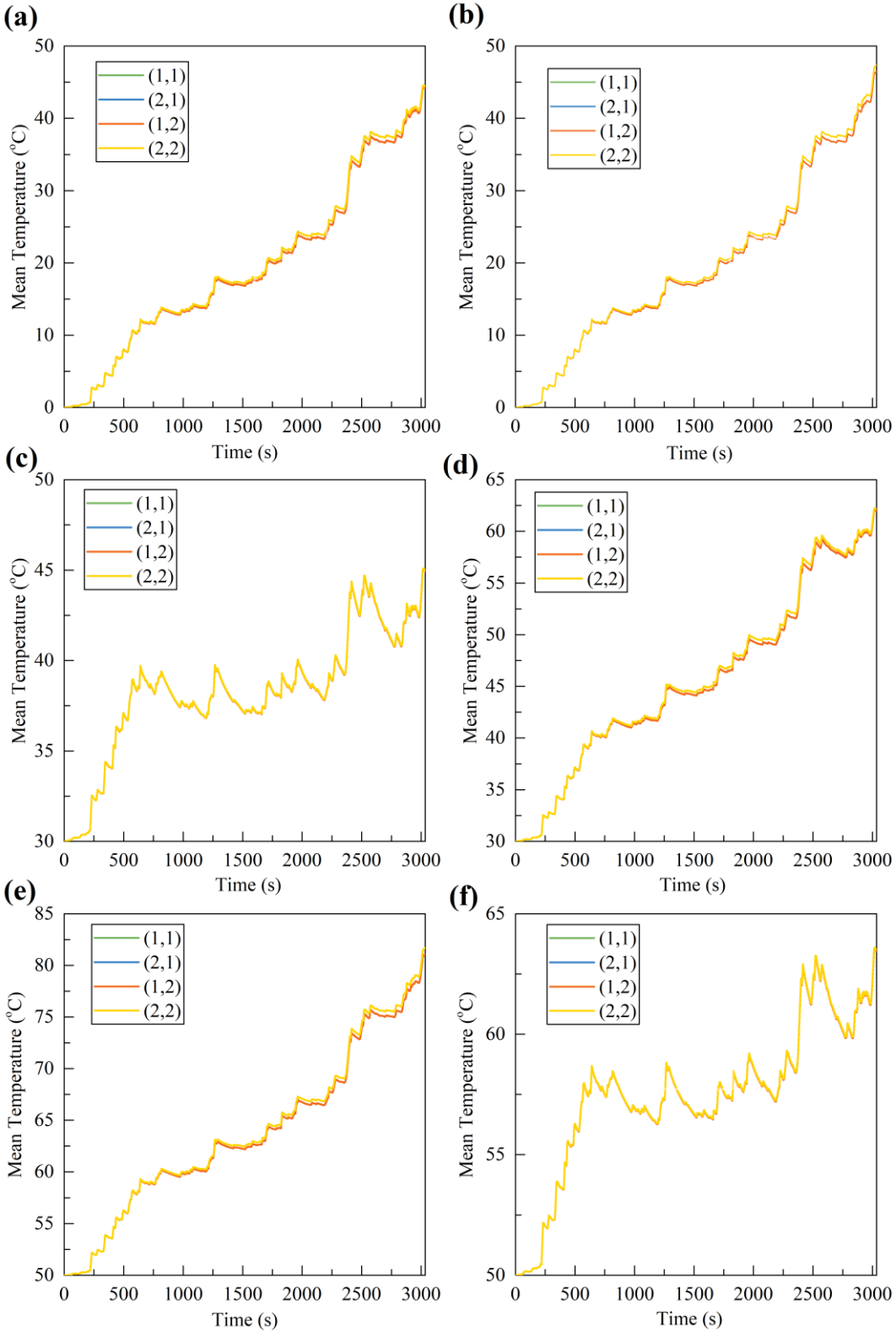

Fig. 11A Mean temperature curves of selected cells in the module of PCM cooling: (a) T_{amb} = 0 °C, PCT = 35 °C, (b) T_{amb} = 0 °C, PCT = 55 °C, (c) T_{amb} = 30 °C, PCT = 35 °C, (d) T_{amb} = 30 °C, PCT = 55 °C, (e) T_{amb} = 50 °C, PCT = 35 °C and (f) T_{amb} = 50 °C, PCT = 55 °C

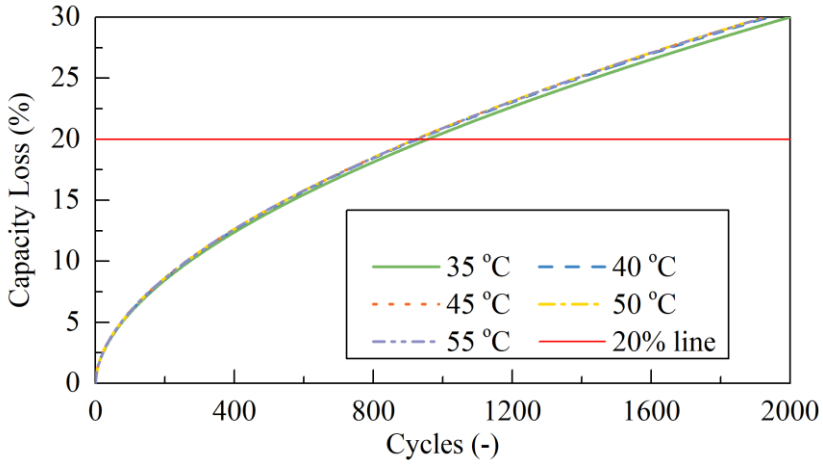

Fig. 12A Capacity loss trajectories of CPM cooling at T_{amb}=0 °C